Cross-validations of the Aeolus aerosol products and new developments with airborne high-spectral-resolution lidar measurements above the tropical Atlantic during JATAC

Trapon, Dimitri; Baars, Holger; Floutsi, Athena Augusta; Bley, Sebastian; Haarig, Moritz; Lacour, Adrien; Flament, Thomas; Dabas, Alain; Ehlers, Frithjof; More Authors

DOI
10.5194/amt-18-3873-2025

Publication date
2025

Document Version
Final published version

Published in
Atmospheric Measurement Techniques

Atmos. Meas. Tech., 18, 3873–3896, 2025
https://doi.org/10.5194/amt-18-3873-2025

Atmospheric Measurement Techniques
Open Access
EGU

Cross-validations of the Aeolus aerosol products and new developments with airborne high-spectral-resolution lidar measurements above the tropical Atlantic during JATAC

Dimitri Trapon[1], Holger Baars[1], Athena Augusta Floutsi[1], Sebastian Bley[1], Moritz Haarig[1], Adrien Lacour[2,3], Thomas Flament[2,4], Alain Dabas[2], Amin R. Nehrir[5], Frithjof Ehlers[6,7], and Dorit Huber[8]

[1]Leibniz Institute for Tropospheric Research (TROPOS), Leipzig, Germany
[2]CNRM, Université de Toulouse, Météo-France, CNRS, Toulouse, France
[3]Magellium, Ramonville-Saint-Agne, Occitanie, France
[4]EUMETSAT, Darmstadt, Germany
[5]NASA Langley Research Center, Hampton, VA, USA
[6]Geoscience and Remote Sensing, Delft University of Technology, Delft, the Netherlands
[7]Collecte Localisation Spatiale (CLS), Observations Spatiales, Ramonville-Saint-Agne, France
[8]DoRIT, Munich, Germany

Correspondence: Dimitri Trapon (dimitri.trapon@tropos.de)

Received: 31 January 2025 – Discussion started: 10 February 2025
Revised: 15 April 2025 – Accepted: 13 May 2025 – Published: 14 August 2025

Abstract. The Joint Aeolus Tropical Atlantic Campaign (JATAC) conducted in 2022 in Cabo Verde has provided quantitative lidar measurements, particularly from the NASA Langley High-Altitude Lidar Observatory (HALO) on board DC-8 aircraft, for process-level understanding of tropical dynamics, as well as for satellite validation. For the first time, the optical properties of particles (i.e. backscatter, extinction, attenuated backscatter coefficients, and depolarization ratios) have been measured for extended tropospheric sections collocated with the Aeolus satellite overpasses with limited geolocation and time offsets. This has contributed to the evaluation of the Aeolus Level-2A (L2A) aerosol optical properties product. In addition, localized aerosol profiles were measured by the ground-based multiwavelength Raman polarization and water vapour lidar Polly^{XT}.

In this study, we assess the quality of the Aeolus L2A product retrieved with the standard correct algorithm (SCA) and the maximum likelihood estimation (MLE) as part of the September 2022 dataset reprocessed with the L2A processor, version 16. The focus is given to the 355 nm aerosol retrievals given at finer horizontal resolution, i.e. the so-called Aeolus measurement level at ≈ 18 km. They are compared to the 532 nm HALO airborne profiles that are converted to 355 nm using the backscatter Ångström exponent. HALO and Polly^{XT} polarization lidars also provide insights into the L2A algorithm's limitations when looking at non-spherical particles such as Saharan dust. Even though it has no cross-polarized component, the Aeolus measurements can be corrected using collocated observations with such instruments that include both co-polarized and cross-polarized components of the backscattered light. Moreover the cross-validation with independent lidar measurements enables estimation of the lower limits for Aeolus backscatter detection.

1 Introduction

The Aeolus Level-2A (L2A) aerosol optical properties product (Flament et al., 2021), processed from the first ultraviolet (UV) Doppler lidar in space ALADIN (Atmospheric LAser Doppler INstrument), has been gradually improved since its first implementation following the launch of the mission in 2018. Initially referred to as a spin-off product, the validity of its independent retrieval of the extinction and backscatter coefficients for particles (Ansmann et al., 2009; Flamant et al., 2008) was demonstrated using independent datasets

for validation (Abril-Gago et al., 2022; Gkikas et al., 2023) and scientific applications (Baars et al., 2021; Khaykin et al., 2022).

In particular, the use of aerosol retrievals from the so-called standard correct algorithm (SCA), developed at Institut Pierre Simon Laplace (IPSL) and Météo-France, revealed limitations (Baars et al., 2020). This first algorithm corresponds to a direct inversion of the lidar equations without a priori conditions and is highly affected by noise (Flament et al., 2021). The primary mission of Aeolus was to measure vertical profiles of the Earth's winds at the global scale, from the surface up to the lower stratosphere. The vertical range bins are limited to 24 and from 250 m to 2 km thickness, reaching from the ground to a maximum altitude of 30 km. The first objective was to focus on aerosol-free regions of the atmosphere with an atmospheric signal by molecules from the Rayleigh channel. Because of the attenuation of the laser beam due to the overlying molecular atmosphere, the signal-to-noise ratio (SNR) decreases with decreasing altitude, with the smaller values corresponding to the lowest-range bins.

Every version of the L2A processor was released typically every six months during the operational phase of the Aeolus mission. Together with the technical documentation, each processor version forms an L2A product level labelled as "Baseline". A new algorithm was developed using physically constrained optimal estimation to compensate for the noisy signals, especially when deriving the extinction coefficients. This new algorithm, called maximum likelihood estimation (MLE) (Ehlers et al., 2022), was implemented through the L2A processor labelled Baseline 15 by September 2022. The MLE was initially processed on the coarser Aeolus horizontal resolution, i.e. referred to as a basic repeat cycle (BRC) or observation, and resulted from a signal accumulation over ≈ 90 km, to be aligned with the SCA algorithm. Later, it was decided to provide the MLE at a sub-BRC level with a higher horizontal resolution ≈ 18 km. These retrievals are labelled MLEsub within the L2A product Baseline 16. The L2A algorithms SCA and MLE were maintained and improved at Météo-France until Baseline 15, the activities being transferred to the Leibniz Institute for Tropospheric Research (TROPOS) by Baseline 16.

The Aeolus dataset corresponding to the 2022 Joint Aeolus Tropical Atlantic Campaign (JATAC) has been processed with Baseline 16 as part of the fourth reprocessing campaign activities conducted by the Aeolus Data, Innovation, and Science Cluster (DISC). A summary of the quality of Aeolus data products can be downloaded from https://earth.esa.int/eogateway/documents/d/earth-online/aeolus-summary-reprocessing-4-fm-b-disc-2024-04-30 (last access: 17 January 2025). The reprocessed dataset makes it possible to assess the performance of both SCA and newly implemented MLEsub algorithms using independent lidar measurements. The present study focuses on cross sections of the atmosphere up to an altitude ≈ 10 km observed by the High-Altitude Lidar Observatory (HALO) (Carroll et al., 2022; Nehrir et al., 2018) on board NASA's DC-8 remote sensing aircraft (Bedka et al., 2021; Nehrir et al., 2017) flying towards the north and collocated with Aeolus ascending overpasses above the East Atlantic Ocean. The small geolocation offset (i.e. less than 6 km) and time offset (i.e. less than an hour) between DC-8 flights and Aeolus offer a unique opportunity to compare both Aeolus ALADIN and DC-8 HALO continuous measurements of aerosol optical properties with very close collocation. In addition, direct profiles above Mindelo, Cabo Verde, are selected to be compared with aerosol retrievals from ground-based multiwavelength Raman polarization and water vapour lidar Polly^{XT} (Baars et al., 2016; Engelmann et al., 2016). Combining measurements from satellite, aircraft-based, and ground-based instruments enables obtaining a complete picture of tropospheric aerosols. Independent retrievals of the aerosol depolarization ratio provided by HALO and Polly^{XT} also help in understanding how the cross-polarized component of the light missed by Aeolus impacts the L2A aerosol retrievals (Gkikas et al., 2023). The Cabo Verde region is indeed known to be affected by highly depolarizing particles such as Saharan dust (Haarig et al., 2022; Rittmeister et al., 2017). The HALO and Polly^{XT} observations will support further refinement of Aeolus products and may complement the classification database for dominant aerosol type.

The Aeolus mission was part of the ESA Earth-Observation Programme as a demonstrator of wind lidar technology. In addition to the proof of concept for a first UV Doppler lidar in space (Dabas et al., 2008), the mission objectives include evaluation of the high spectral resolution (HSR) capacity of the ALADIN instrument. Aeolus is indeed able to separate the contributions from molecules and particles, contrary to elastic backscatter lidars such as CALIOP on board NASA/CNES CALIPSO (Winker et al., 2009). This results in no ambiguities in aerosol and cloud optical properties and no requirements for a priori hypotheses on the extinction-to-backscatter ratio, i.e. the so-called lidar ratio. A key advantage of the Aeolus measurement is also the simultaneous aerosol and wind lidar profiling. The cross-comparison of Aeolus L2A data with independent aerosol retrievals is in anticipation of subsequent missions such as EarthCARE (Illingworth et al., 2015) and Aeolus-2. Moreover, the quality assessment of the Aeolus aerosol product has been mainly achieved with localized ground-based measurement (Abril-Gago et al., 2022; Gkikas et al., 2023; Paschou et al., 2022) during the operational phase until successful re-entry into Earth's atmosphere during summer 2023. The present study offers a unique opportunity to analyse longer atmospheric sections up to 626 km long collocated with aircraft observation in various atmospheric conditions.

In this paper, the Aeolus L2A SCA and MLE algorithms and JATAC are introduced. Then, the NASA HALO lidar observations performed during the Convective Processes Experiment – Cabo Verde (CPEX-CV) airborne field campaign

(Nowottnick et al., 2024) are presented. The wavelength conversion of the HALO measurements and re-gridding to match Aeolus sampling are described, followed by a results section firstly showing direct profiles above Mindelo, Cabo Verde, observed by Aeolus and HALO with ground-based lidar Polly^{XT}. Then, the cross-comparison of the tropospheric sections between Aeolus and re-gridded HALO is described. The final section concludes the paper, summarizing the L2A algorithm performance and sharing recommendations for future applications. This will be appreciated by the atmospheric science community, as Aeolus data have been gradually disseminated to the public since 2021, encouraging scientific studies using the dataset.

2 Lidar measurements above the Atlantic in the context of the Aeolus Tropical Campaign 2022

2.1 Aeolus L2A aerosol product: concept of SCA and MLE algorithms

The present paper focuses on the Aeolus L2A aerosol and cloud optical properties product retrieved with the SCA and MLE algorithms.

Standard correct algorithm. The SCA corresponds to a direct inversion of the lidar equations from the accumulated Rayleigh and Mie signals as measured by Aeolus. Making use of the HSR capacity of ALADIN, the attenuated backscatter coefficients for molecules $\beta_{\mathrm{mol}}^{\mathrm{att}}$ and particles $\beta_{\mathrm{part}}^{\mathrm{att}}$ are a result of cross-talk correction of the lidar signals from vertical matching between Rayleigh and Mie channels, i.e. calculated from the backscattered signal and the transmission through the atmosphere, split up into molecule and particle contributions as described in Eqs. (7) and (8) of Flament et al. (2021). The particulate backscatter β_{part} and extinction α_{part} are derived from the cross-talk-corrected products, and the molecular backscatter β_{mol} is related to air density, as shown in Eqs. (9), (10), and (14) of Flament et al. (2021). The particulate backscatter β_{part} and extinction α_{part} are measured independently without a priori conditions (Flamant et al., 2008). The range bins are considered homogeneously populated by particles, and the top bin is assumed to contain no aerosol.

Maximum likelihood estimation. Because the SCA is sensitive to noise, leading to non-physical retrievals in low-SNR regions, a new approach based on optimal estimation was introduced in the L2A processing by Baseline 15. It is referred to as maximum likelihood estimation (MLE) and consists of a reverse processing with derivation of the optical parameters, i.e. the physically modelled state that agrees the most with real signals, as illustrated in Eq. (11) of Ehlers et al. (2022). The MLE approach makes use of the limited memory quasi-Newton L-BFGS-B algorithm (Zhu et al., 1997). Contrary to the SCA, MLE is a constrained processing with physical limits assuming vertical collocation between the extinction and the backscatter. The lidar ratio for particles cannot exceed a range from 2 to 200 sr, and the extinction coefficient must be positive (Ehlers et al., 2022).

The Aeolus L2A product includes aerosol retrievals from multiple algorithms and varying horizontal resolutions. The SCA coarser sampling is the observation level referred to as the BRC ≈ 90 km in the horizontal direction. It corresponds to a signal accumulation of 600 consecutive laser pulses. The so-called "measurements" are the data element resulting from the accumulation of less pulses, comprising sub-BRC profiles up to 30. On September 2022, the settings were the following: five consecutive measurements ≈ 18 km correspond to one BRC ≈ 90 km. The SCA particulate and molecular attenuated backscatters are aligned with the measurement level, and the other SCA products (e.g. extinction and backscatter coefficients for particles) are aligned with the BRC level. The BRC level products are affected by uncertainties, as the averaging may encompass signals from different conditions (e.g. broken clouds and a non-homogeneous aerosol layer).

The aerosol retrievals derived with the MLE algorithm were initially aligned with the BRC level. The L2A development team decided to provide the MLE at a finer-horizontal-resolution sub-BRC, i.e. measurement level by Baseline 16. JATAC 2022 then enables assessing both SCA and MLEsub products aligned with this sub-BRC resolution. Figure 1 illustrates the difference between an Aeolus BRC and the sub-BRC sampling: the ground track for one BRC ≈ 90 km is shown in Fig. 1a (green), and the five corresponding sub-BRC measurements ≈ 18 km are illustrated in Fig. 1b.

The L2A products selected for the study are the SCA particulate attenuated backscatter coefficient $\beta_{\mathrm{part}}^{\mathrm{att}}$, the MLEsub backscatter coefficient for particles β_{part}, and the MLEsub extinction coefficient for particles α_{part}. The quality check (QC) flags provided for MLEsub retrievals have been applied. They are based on SNR and error estimate thresholds described in detail in the L2A user guide version 2.2 (Trapon et al., 2022). It must be noted that Baseline 16 does not include QC flags for SCA particulate attenuated backscatter, which then contains non-physical values (i.e. negative up to 40 %) because of non-perfect cross-talk correction. The negative values are distributed in low SNR regions with aerosol-free conditions. It was decided to flag the negative values for the study.

2.2 The Joint Aeolus Tropical Atlantic Campaign (JATAC)

JATAC was instigated by the European Space Agency (ESA) in Cabo Verde from June to September of 2021 and 2022. It aimed at providing reference atmospheric measurements to validate ESA Aeolus wind and aerosol products retrieved at 355 nm and prepare upcoming ESA Earth Explorer missions such as EarthCARE (Illingworth et al., 2015). JATAC also addressed scientific objectives regarding long-range transport of Saharan dust particles, e.g. investigating their re-

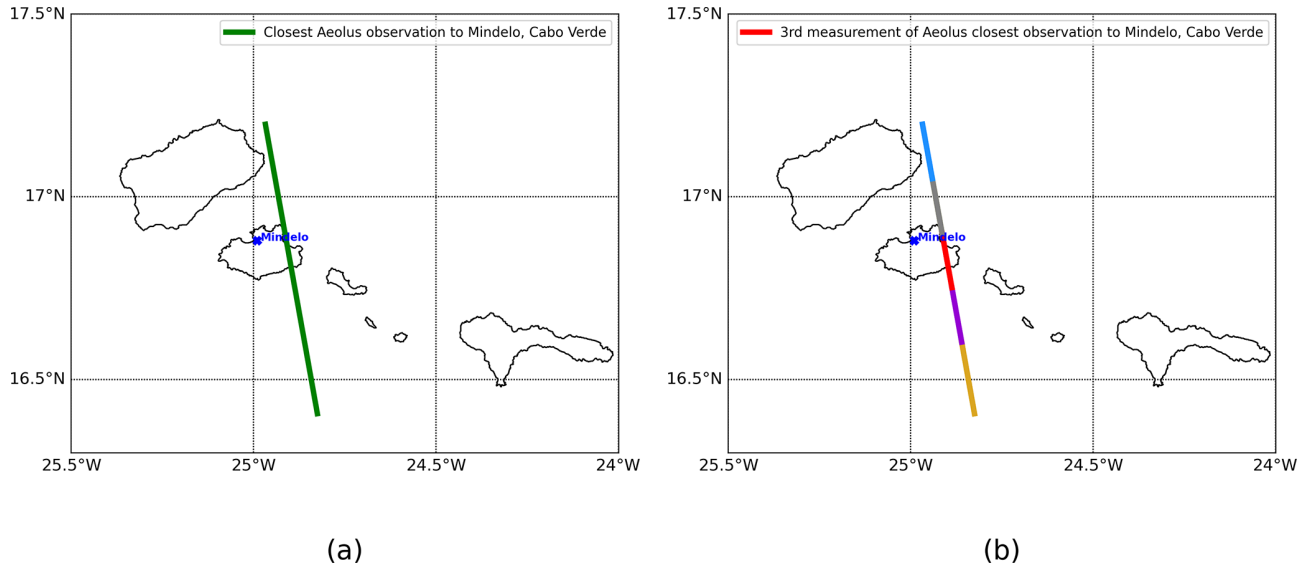

Figure 1. Illustration of Aeolus coarser horizontal sampling BRC (observation ≈ 90 km) **(a)** and corresponding sub-BRC profiles (measurement ≈ 18 km) **(b)** on 16 September 2022.

lation to the formation of convective systems and improving climate and numerical weather prediction models (Fehr et al., 2023; Flamant et al., 2024). The science objectives were covered through simultaneous observations of multiple aircraft collocated with Aeolus overpasses and ground-based cloud and aerosol measurements, including radiosondes and dropsondes. The ground-based instruments were operated at Ocean Science Center Mindelo, Cabo Verde, in 2021 and 2022. This includes the multiwavelength Raman polarization and water vapour lidar Polly^{XT} (Baars et al., 2016; Engelmann et al., 2016), the eVe reference polarization lidar (Paschou et al., 2022), and a W-band Doppler cloud radar. The Airborne Demonstrator for the Direct-Detection Doppler Wind Lidar ALADIN (Lemmerz et al., 2023) on board the DLR Falcon-20 aircraft was deployed in September 2021, as well as the high-spectral-resolution Doppler lidar (LNG) (Bruneau et al., 2015) on board the SAFIRE Falcon-20 aircraft. The Aerovizija Advantic WT-10 light aircraft with optical particle spectrometers, filter photometers, and nephelometers for in situ aerosol characterization was deployed in 2021 and operated during two weeks in September 2022 (Fehr et al., 2023).

3 NASA's Convective Processes Experiment – Cabo Verde (CPEX-CV)

3.1 NASA DC-8 aircraft and flights above Cabo Verde

NASA CPEX-CV (Nowottnick et al., 2024; Zawislak et al., 2022) is a continuation of the CPEX (Turk et al., 2020) and CPEX – Aerosol & Winds (CPEX-AW) (https://asdc.larc.nasa.gov/project/CPEX-AW, last access: 11 April 2025, https://www.earthdata.nasa.gov/data/projects/cpex-aw, last access: 11 April 2025) campaigns, both conducted in the tropical East Atlantic in 2017 and 2021, respectively. One key objective was to study the atmosphere dynamics in order to interpret spaceborne remote measurement of tropospheric aerosols as part of JATAC 2022. CPEX-CV consisted of the deployment of NASA's DC-8 aircraft out of Sal island, Cabo Verde, during the summer of 2022.

Some flights of the DC-8 have been specifically designed to include a collocated section with the Aeolus overpasses. Figure 2 illustrates the ground track of the Aeolus orbits for September 2022, with the NASA DC-8 aircraft flying below the satellite in the same direction toward the north for the ascending overpasses only (i.e. Fig. 2: (a) green, (b) rose). Three scenes up to 626 km long are presented in this study and correspond to 9, 15, and 16 September 2022. The scenes of 9 and 16 September 2022 correspond to Friday ascending overpasses (Fig. 2b, rose), with the closest profile to Mindelo, Cabo Verde, at ≈ 19:33 UTC. The scene of 15 September 2022 corresponds to the Thursday ascending overpass (Fig. 2a, green), with the closest profile to Mindelo, Cabo Verde, at ≈ 19:20 UTC.

3.2 NASA Langley High-Altitude Lidar Observatory (HALO) and 532 nm aerosol products

The NASA HALO on board the DC-8 aircraft was operated during CPEX-CV, which was a part of JATAC 2022. It is a differential absorption lidar (DIAL) and HSR lidar (HSRL) with multiple configurations, including water vapour DIAL and HSRL and methane DIAL and HSRL (Barton-Grimley et al., 2022; Bedka et al., 2021;

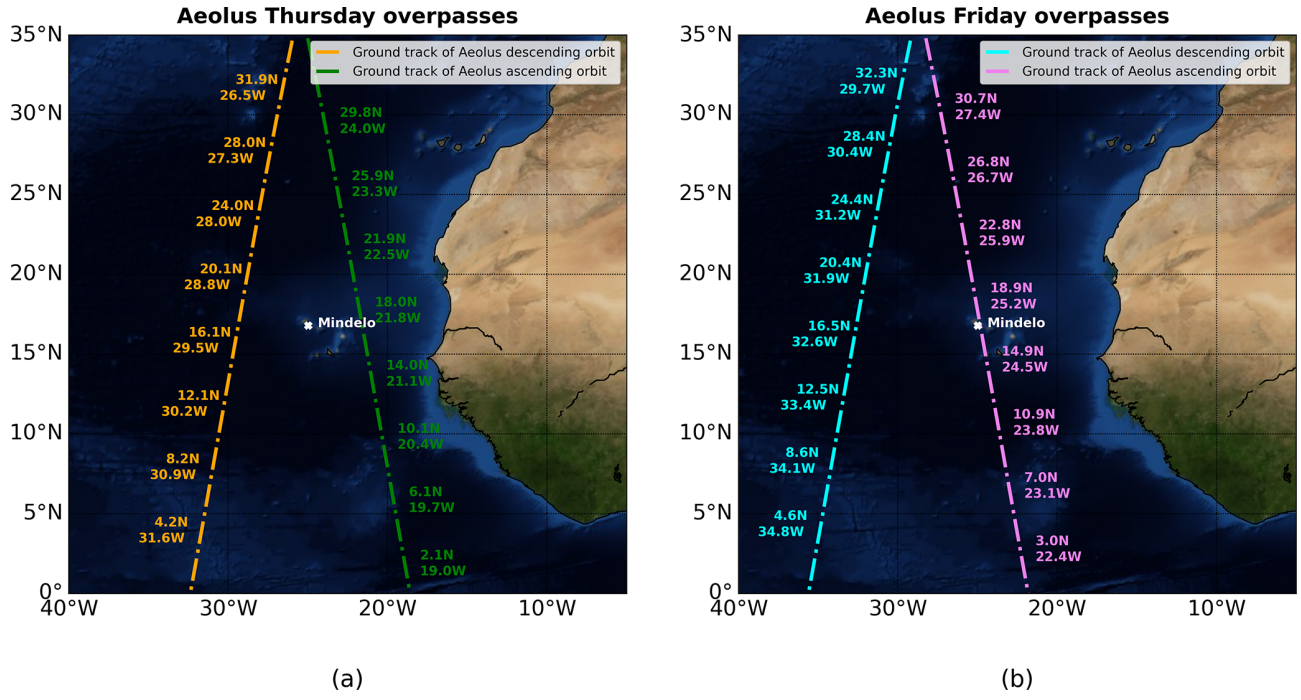

Figure 2. Closest overpasses of Aeolus to Cabo Verde in September 2022 (Blue Marble collection used for background map; courtesy of https://visibleearth.nasa.gov/, last access: 11 April 2025).

Carroll et al., 2022; Nehrir et al., 2017, 2018). For CPEX-CV, HALO operated in the water vapour DIAL and HSRL configurations to retrieve water vapour profiles as well as profiles of optical properties of atmospheric aerosols from multiple wavelength observations (532, 1064 nm). HALO does not emit UV signals at 355 nm like Aeolus ALADIN, and a wavelength conversion is therefore required when carrying out comparisons. The spectral dependence of optical properties for desert dust is known to be less pronounced between 355 and 532 nm than between 355 and 1064 nm (Burton et al., 2015; Groß et al., 2013, 2015; Haarig et al., 2017b, 2018; Hofer et al., 2017). Therefore, HALO products at 532 nm are preferred over the products at 1064 nm for the conversion to 355 nm. Moreover, HALO transmits linear polarization, whereas Aeolus transmits circular polarization. Therefore, the circular aerosol depolarization ratio is derived from the HALO ready-to-use linear aerosol depolarization ratio at 532 nm. HALO aerosol extinction and backscatter coefficients, respectively labelled $\alpha_{\mathrm{aer},532}$ and $\beta_{\mathrm{aer},532}$, are taken as input for the cross-comparison with the MLEsub retrievals. The HALO attenuated backscatter coefficient at 532 nm, labelled $\beta^{\mathrm{att}}_{\mathrm{aer},532}$, is selected for the cross-comparison with the SCA retrievals. The HALO total scattering ratio at 532 nm, labelled R_{532}, HALO linear aerosol depolarization ratio at 532 nm, labelled $\delta_{\mathrm{lin},532}$, and HALO dominant aerosol type product based on Burton et al. (2012) typing algorithms are used as the third variable distribution in the two-dimensional histograms with a colour map.

The calculation of the HALO 532 nm ready-to-use products is described within the HALO documentation as below and in more detail in Hair et al. (2008).

The aerosol extinction coefficient at 532 nm is determined as follows:

$$\alpha_{\mathrm{aer},532} = -\frac{1}{2}\frac{\partial}{\partial r}\ln\left\{\frac{r^2 P^{\parallel}_{\mathrm{mol}}}{F\psi\beta_{\mathrm{mol},532}}\right\} - \alpha_{\mathrm{mol},532}, \quad (1)$$

with $\beta_{\mathrm{mol},532}$ being the molecular backscatter coefficient at 532 nm, $\alpha_{\mathrm{mol},532}$ the molecular extinction coefficient at 532 nm, r the range from the DC-8 aircraft to the measurement bin, F the transmission of the molecular scattering through the iodine filter, ψ the transmitter-to-receiver overlap function (which is considered unity beyond the 1.0 km range from the aircraft), and $P^{\parallel}_{\mathrm{mol}}$ the filtered molecular scattering channel measured through the iodine vapour filter.

The aerosol backscatter coefficient at 532 nm can be found as follows:

$$\beta_{\mathrm{aer},532} = \beta^{\parallel}_{\mathrm{aer},532} + \beta^{\perp}_{\mathrm{aer},532}, \quad (2)$$

with $\beta^{\perp}_{\mathrm{aer},532}$ being the perpendicular (cross-polarized) aerosol backscatter coefficient at 532 nm and $\beta^{\parallel}_{\mathrm{aer},532}$ the parallel (co-polarized) aerosol backscatter coefficient at 532 nm.

The linear aerosol depolarization ratio at 532 nm is determined as follows:

$$\delta_{\mathrm{lin},532} = \frac{\beta^{\perp}_{\mathrm{aer},532}}{\beta^{\parallel}_{\mathrm{aer},532}}. \quad (3)$$

The total scattering ratio at 532 nm is found as follows:

$$R_{532} = \frac{\beta_{\text{aer},532}}{\beta_{\text{mol},532}} + 1, \tag{4}$$

where $\beta_{\text{aer},532}$ is the aerosol backscatter coefficient at 532 nm.

4 Methodology

4.1 Conversion of the HALO 532 nm atmospheric products to parallel 355 nm

Aeolus ALADIN transmits circularly polarized light. The conversion of the HALO signal to 355 nm then implies deriving the circular aerosol depolarization ratio at 532 nm using equation (A14) from Paschou et al. (2022):

$$\delta_{\text{circ},532} = \frac{2 \times \delta_{\text{lin},532}}{1 - \delta_{\text{lin},532}}. \tag{5}$$

Aeolus measures only the co-polarized component of the backscattered light, i.e. parallel to the transmitted polarization. Therefore, to be fairly compared with Aeolus, the HALO parallel-only aerosol backscatter 532 nm coefficient $\beta^{\parallel}_{\text{aer},532}$ is derived from Eqs. (2), (3), and (5):

$$\beta^{\parallel}_{\text{aer},532} = \frac{\beta_{\text{aer},532}}{\delta_{\text{circ},532} + 1}. \tag{6}$$

$\delta_{\text{lin},532}$ and the derived $\delta_{\text{circ},532}$ include Not a Number (NaN) values, which represent noisy retrievals below the value of zero depolarization. It was decided to replace these NaN values with 0. This allows assessment of the Aeolus algorithm performance even for regions of the atmosphere without depolarizing particles.

It is necessary to convert the HALO 532 nm aerosol backscatter $\beta_{\text{aer},532}$ and extinction $\alpha_{\text{aer},532}$ to 355 nm using Eqs. (1) and (3) of Ansmann et al. (2002) below, where $\lambda 1 < \lambda 2$, $\gamma_{\beta,\lambda 1,\lambda 2}$ is the backscatter-related Ångström exponent, and $\gamma_{\alpha,\lambda 1,\lambda 2}$ is the extinction-related Ångström exponent:

$$\gamma_{\beta,\lambda 1,\lambda 2} = -\frac{\ln[\beta_{\lambda 1}/\beta_{\lambda 2}]}{\ln(\lambda 1/\lambda 2)}, \tag{7}$$

$$\gamma_{\alpha,\lambda 1,\lambda 2} = -\frac{\ln[\alpha_{\lambda 1}/\alpha_{\lambda 2}]}{\ln(\lambda 1/\lambda 2)}. \tag{8}$$

Then, the HALO 355 nm parallel aerosol backscatter $\beta^{\parallel}_{\text{aer},355}$ and extinction coefficient $\alpha_{\text{aer},355}$ can be derived from Eqs. (7) and (8):

$$\beta^{\parallel}_{\text{aer},355} = \exp\left[\ln\left(\beta^{\parallel}_{\text{aer},532}\right) - \gamma_{\beta,355,532} \ln\left(\frac{355}{532}\right)\right], \tag{9}$$

$$\alpha_{\text{aer},355} = \exp\left[\ln\left(\alpha_{\text{aer},532}\right) - \gamma_{\alpha,355,532} \ln\left(\frac{355}{532}\right)\right]. \tag{10}$$

The backscatter-related Ångström exponent $\gamma_{\beta,355,532}$ and extinction-related Ångström exponent $\gamma_{\alpha,355,532}$ have been measured continuously by Polly$^{\text{XT}}$ at Mindelo. The profiles of the optical properties measured by the Polly$^{\text{XT}}$ are cloud-screened and quality assured. A Saharan air layer (SAL) was frequently observed between heights of 1.5 and 4.0 km.

During 9 September 2022, a median $\gamma_{\beta,355,532}$ of −0.39 (−0.51 and −0.31 are the 25th and 75th percentiles, respectively) was derived in this height range (SAL) from three profiles during nighttime. On the same day and in the same height range, a median $\gamma_{\alpha,355,532}$ of −0.09 (−0.5 and 0.43) was derived from two Raman lidar profiles during nighttime. The values in brackets again correspond to the 25th and 75th percentiles. Similarly, median values of 0 (−0.01 and 0.02) for $\gamma_{\beta,355,532}$ (three nighttime profiles) and 0.06 (0.03 and 0.12) for $\gamma_{\alpha,355,532}$ (three nighttime profiles) have been estimated by Polly$^{\text{XT}}$ for the height range of 0.8–1.0 km corresponding to the planetary boundary layer (PBL).

During 15 September 2022, a median $\gamma_{\beta,355,532}$ of −0.44 was derived in the SAL height range from one profile during nighttime. On the same day and in the same height range, a median $\gamma_{\alpha,355,532}$ of 0.06 (−0.48 and 0.58) was derived from three Raman lidar profiles during nighttime. Similarly, median values of 0.23 for $\gamma_{\beta,355,532}$ (one nighttime profile) and 0.14 (0.01 and 0.22) for $\gamma_{\alpha,355,532}$ (five nighttime profiles) have been estimated by Polly$^{\text{XT}}$ for the PBL height range.

During 16 September 2022, a median $\gamma_{\beta,355,532}$ of −0.43 (−0.68 and -0.25) was derived in the SAL height range from nine profiles during nighttime. On the same day and in the same height range, a median $\gamma_{\alpha,355,532}$ of 0.11 (−0.21 and 0.48) was derived from 11 Raman lidar profiles during nighttime. Similarly, median values of 0.31 (0.17 and 0.41) for $\gamma_{\beta,355,532}$ (nine nighttime profile) and 0.24 (0.13 and 0.38) for $\gamma_{\alpha,355,532}$ (16 profiles) have been estimated by Polly$^{\text{XT}}$ for the PBL height range.

The close-to-zero extinction-related Ångström exponent and negative backscatter-related Ångström exponent are known to be representative of mineral dust (Floutsi et al., 2023; Gebauer et al., 2024; Haarig et al., 2022). For the present study, the SAL values are applied from the 1.5 km altitude to the top altitude of 10 km, as the HALO dominant aerosol type product reveals similar aerosol load below and above 4 km in altitude (see Figs. A1, A2, and A3) and because the impact on the tropospheric background in aerosol-free regions is assumed to be minor. The PBL values are applied for the section going from the ground to an altitude of 1.5 km.

The HALO 355 nm attenuated backscatter coefficient for particles $\beta^{\text{att}\parallel}_{\text{aer},355}$ can be calculated with Eqs. (9) and (10) as follows:

$$\beta^{\text{att}\parallel}_{\text{aer},355} = \beta^{\parallel}_{\text{aer},355}(R) \exp\left[-2 \int_{z_{\text{aircraft}}}^{z} \left(\alpha_{\text{mol},355}(y) + \alpha_{\text{aer},355}(y)\right) \mathrm{d}y\right], \tag{11}$$

with R being the DC-8 aircraft range-to-target, dy the range bin thickness, z_{aircraft} the Global Positioning System (GPS) altitude of the DC-8 aircraft, z the altitude of the mean sea level, and $\alpha_{\text{mol},355}$ the molecular extinction coefficient for dry air. $\alpha_{\text{mol},355}$ below the DC-8 is derived from pressure p (hPa) and temperature T (K) measured by HALO. Equation (4.6) of the Aeolus Level 2A Algorithm Theoretical Basis Document (ATBD) (Flamant et al., 2022) shown below has been used for the calculation of $\alpha_{\text{mol},355}$ using a coefficient of 1.16, which was determined experimentally (Collis and Russell, 1976).

$$\alpha_{\text{mol},355}(y) = 1.16\left(\frac{550}{355}\right)^{4.09}\frac{p(y)}{1013}\frac{288}{T(y)}10^{-5} \tag{12}$$

The molecular extinction above the DC-8 up to 80 km in altitude is calculated using the same equation with pressure and temperature information from the numerical weather prediction (NWP) model from the European Centre for Medium-Range Weather Forecasts (ECMWF). It has to be noted that the flight altitude of the DC-8 is constant enough for the three collocated sections selected for the study to neglect variations. A mean value of $5.0 \times 10^{-4}\,\text{m}^{-1}$ has been calculated for the molecular extinction above the DC-8 and used as a constant for all scenes. This constant is added to the $\alpha_{\text{mol},355}$ derived in Eq. (12) when calculating the $\beta^{\text{att}\parallel}_{\text{aer},355}$ in Eq. (11).

Aeolus MLEsub extinction and backscatter coefficients for particles and the SCA particulate attenuated backscatter coefficient can then be compared with the 355 nm converted HALO atmospheric products. Only the valid bins with positive values are considered for the statistics (i.e. the invalid measurements coded as NaN in one product are ignored in the second dataset and vice-versa). The flagging of the negatives is applied for all Aeolus and HALO products used in the cross-comparisons. The HALO and Aeolus cloud masks are not applied to keep as many valid bins as possible. This helps in assessing how well Aeolus observes Saharan dust and the mixture of aerosol and cloud, the HALO dominant aerosol type product being used as ad-hoc classification.

4.2 HALO re-gridding onto Aeolus sampling

One of the major advantages of Aeolus is the adjustable vertical sampling with range bin settings (RBS). Specific settings have then been set for the region of interest over the Atlantic covering latitudes 12 to 22° N and longitudes 19 to 31° W. The top height bin stops at ≈ 18 km in altitude, and the following vertical samplings have been applied: 500 m from 0 to ≈ 2 km in altitude, 750 m from ≈ 2 to ≈ 8 km in altitude, 1000 m from ≈ 8 to ≈ 18 km in altitude. The horizontal sampling is aligned with ≈ 90 km for the coarser observation level BRC and with ≈ 18 km for finer sub-BRC level measurement used for the comparison with HALO data.

The HALO 532 nm channels are sampled at 0.5 s temporal and 1.25 m vertical resolutions. The data are digitally filtered to 30 m vertical resolution to further reduce noise and match the vertical resolution of the 1064 nm data products. Aerosol backscatter and depolarization products are further averaged 10 s horizontally, and aerosol extinction products are averaged 60 s horizontally and 300 m vertically. A ready-to-use quality flagging based on the molecular backscatter signal and referred to as mask_low is applied. A cloud identification tag and height named cloud_top_height is used and plotted over HALO atmospheric products (Figs. 5a–c, 7a–c, 9a–c).

The resolutions of the Aeolus ALADIN and DC-8 HALO instruments are then not aligned. Figure 3b illustrates the Aeolus finer horizontal resolution, i.e. the so-called measurement level (solid black lines), superimposed over the HALO 532 nm aerosol backscatter coefficient. Then, 225 consecutive HALO profiles covering a collocated section ≈ 538 km on 16 September 2022 correspond to six Aeolus BRC profiles (Fig. 3a) and 30 Aeolus measurement profiles (Fig. 3b). With the focus given to Aeolus performance, the HALO atmospheric products are re-gridded onto the coarser Aeolus measurement scale. The HALO 355 nm converted aerosol extinction $\alpha_{\text{aer},355}$, the HALO 355 nm converted parallel aerosol backscatter $\beta^{\parallel}_{\text{aer},355}$, and the HALO 355 nm converted attenuated backscatter for particles $\beta^{\text{att}\parallel}_{\text{aer},355}$ are then re-gridded onto the Aeolus grid by deriving the arithmetic mean per range bin for each profile. The equation below corresponds to the HALO 355 nm aerosol backscatter averaged over the Aeolus grid illustrated in Fig. 3b:

$$\beta_{\text{iAeolus}}\left(\text{Mm}^{-1}\,\text{sr}^{-1}\right) = \frac{\sum \beta_{\text{iHALO}}\left(\text{Mm}^{-1}\,\text{sr}^{-1}\right)}{N}, \tag{13}$$

where N is the number of HALO bins (iHALO) included per Aeolus range bin (iAeolus).

Invalid HALO measurements that correspond to localized conditions, e.g. below dense clouds or within the PBL, and reported as NaN values in the ready-to-use products are not taken into account in the re-gridding. The re-gridding is then performed even where the Aeolus coarser grid encompasses valid and invalid HALO retrievals (e.g. white section of HALO $\beta_{\text{aer},532}$ close to profile 114 [15.7° N–24.7° W] in Fig. 3b), hence a gap filling. The cross-comparison between Aeolus and HALO could then be considered less representative for such conditions if compared to a fully valid bin. Moreover, the atmospheric conditions above the DC-8 aircraft are analysed using Aeolus aerosol products, and only the tropospheric sections with clear sky conditions above the DC-8 are considered for the study. This enables rejecting collocated profiles where the Aeolus signal can be expected to be attenuated.

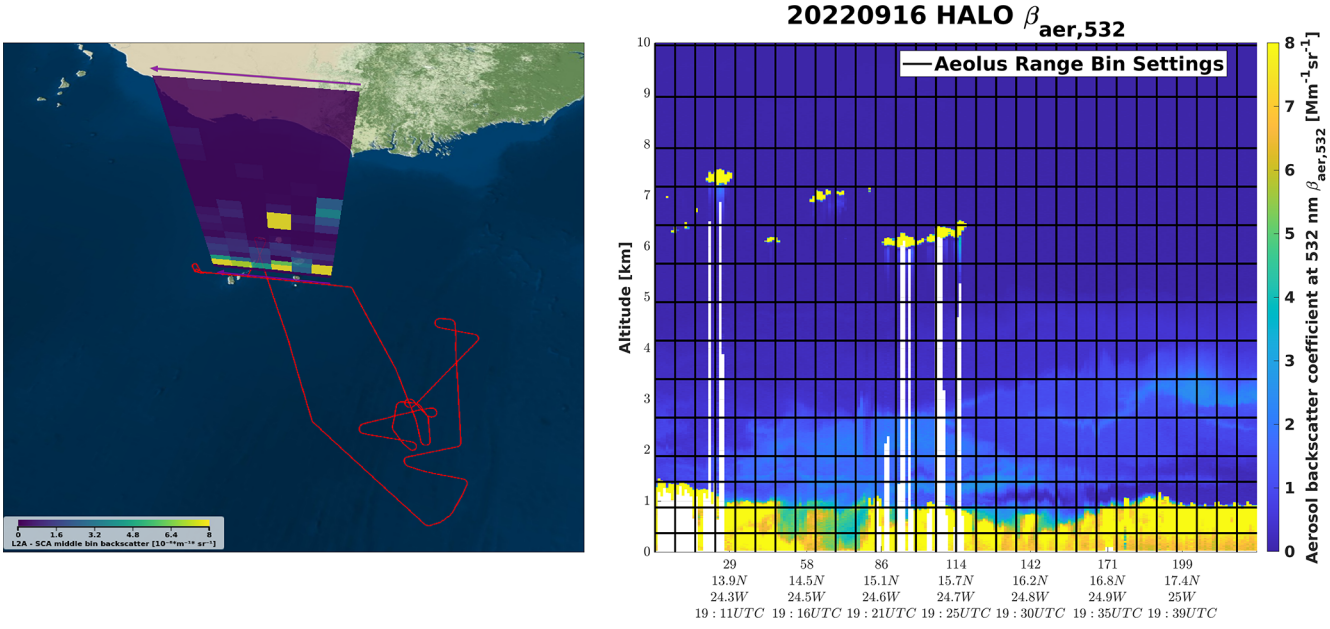

Figure 3. Aeolus direct ascending overpass above Cabo Verde through ESA's VirES (courtesy of https://aeolus.services/, last access: 7 August 2023) on 16 September 2022 (a) showing the backscatter coefficient for particles derived with the SCA (averaged over consecutive vertical bins and referred to as the middle bin). The horizontal resolution is aligned with a coarser BRC level ≈ 90 km. The six consecutive BRC profiles of the Aeolus orbit file no. 23562 are displayed **(a)**. The top altitude is restricted to 10 km, and the range bins are not displayed in scale vertically. The six Aeolus BRC profiles correspond to 30 measurements given at a sub-BRC level ≈ 18 km **(b)**. The Aeolus sub-BRC grid is illustrated in panel **(b)** with solid black lines. The NASA DC-8 flight track of the same day is superimposed in red **(a)**. The HALO aerosol backscatter coefficient at 532 nm $\beta_{aer,532}$ measured for 225 consecutive profiles is shown in panel **(b)**.

5 Results

5.1 Intercomparison of aerosol profiles collocated with a ground-based instrument

The HALO atmospheric product converted to 355 nm has been compared to Aeolus for three case studies on 9, 15, and 16 September 2022. These three case studies correspond to collocated sections with continuous measurement of, respectively, ≈ 626, ≈ 537, and ≈ 538 km long. Figures 4a, A4a, and A5a illustrate how the Aeolus MLEsub β_{part} up to 18 km in altitude helps assess the particle-free conditions above the DC-8 aircraft flying at an altitude ≈ 10 to 11 km. No backscatter signal corresponding to aerosol layers or clouds can be observed above 10 km, confirming the clear sky conditions (e.g. Fig. 4a, with dark blue corresponding to close-to-zero MLEsub β_{part}) above the DC-8. The 2D profiles above Cabo Verde from Aeolus MLEsub and HALO are plotted against ground-based lidar Polly^{XT}. The Polly^{XT} emits linear polarization (Engelmann et al., 2016) with off-nadir ≈ 5°, but Aeolus transmits circularly polarized light. The Polly^{XT} circular aerosol depolarization ratio at 355 nm is then derived to recompute the parallel backscatter coefficient at 355 nm with equations similar to Eqs. (5) and (6). Plotting Polly^{XT} retrievals in addition to Aeolus and HALO for direct profiles above Mindelo, Cabo Verde, enables validation of the wavelength and total to parallel conversions before comparing Aeolus and HALO with the full collocated section. Figure 4b shows the Polly^{XT} total 355 nm backscatter (i.e. red) and parallel 355 nm backscatter (i.e. blue), and illustrates how the HALO total 532 nm backscatter coefficient $\beta_{aer,532}$ (i.e. black) was converted to parallel 355 nm $\beta^{\parallel}_{aer,355}$ (i.e. dark yellow). Both profiles of the parallel 355 nm backscatter retrieved with Raman Polly^{XT} and HALO agree very well with Aeolus MLEsub (i.e. violet) for the SAL from ≈ 2.6 to 4 km in altitude. MLEsub β_{part} of 1.36 ± 0.56 Mm^{-1} sr^{-1} and HALO $\beta^{\parallel}_{aer,355}$ of 1.14 ± 0.02 Mm^{-1} sr^{-1} are measured for the in-core SAL at an altitude of 3 km. The red solid line for Polly^{XT} 355 nm total backscatter represents what Aeolus would see if it would have included a polarization channel, followed by increasing the backscatter signal by a factor ≈ 34 % for the in-core dust layer at 3 km in altitude. When looking at the extinction coefficient for particles, Aeolus MLEsub also agrees with the other instruments even if the Aeolus signal appears to be too much attenuated and therefore flagged below 3 km in altitude. One could notice the high errors for MLEsub α_{part}. Similar observations can be made from the cases of 9 September 2022 (see

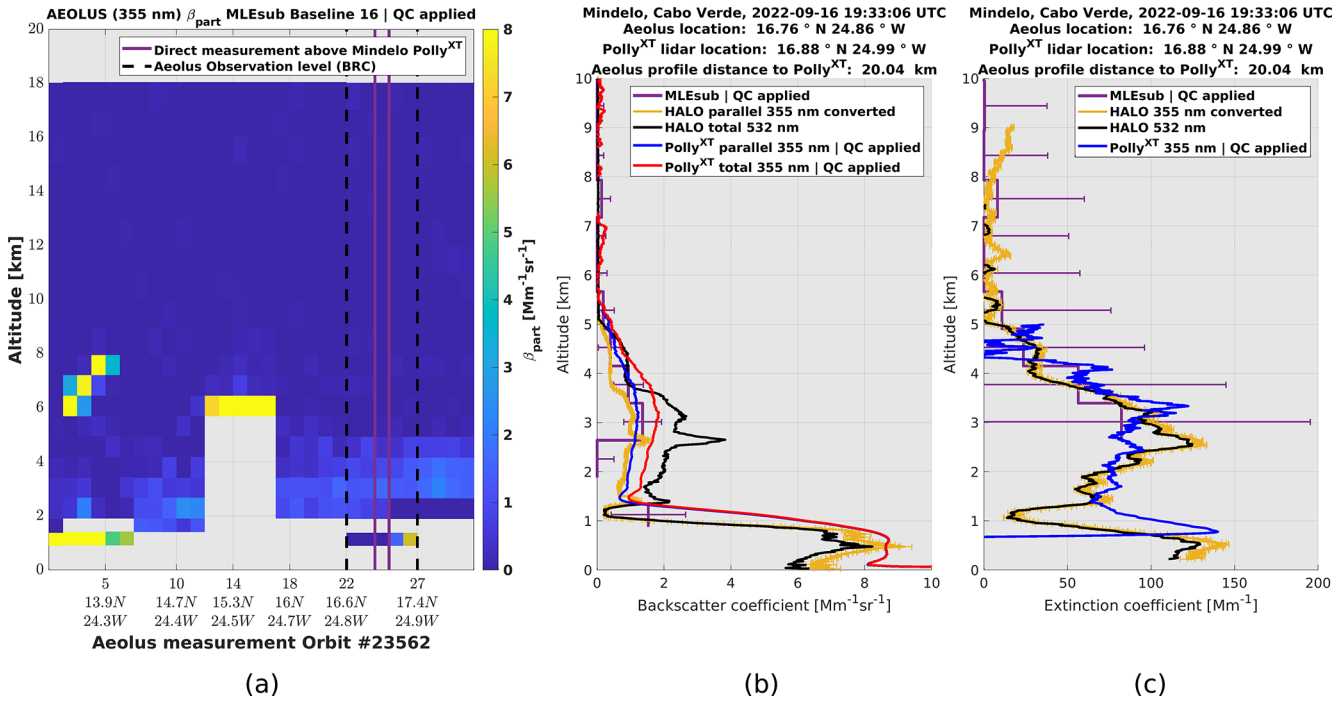

Figure 4. Aeolus MLEsub β_{part} on 16 September 2022 **(a)** and cross-comparison of 2D profiles above Mindelo, Cabo Verde, with HALO and Polly^{XT} for MLEsub β_{part} **(b)** and MLEsub α_{part} **(c)**.

Fig. A4) and 15 September 2022 (see Fig. A5). The Aeolus MLEsub is able to retrieve coherent optical properties in low altitude ≈ 1 km below dust with high backscatter up to $9.45 \pm 2.12\,\text{Mm}^{-1}\,\text{sr}^{-1}$ (see Fig. A4b), even if this looks overestimated when compared to the other instrument retrievals below $7.0\,\text{Mm}^{-1}\,\text{sr}^{-1}$. The Aeolus MLEsub gives coherent backscatter values for a dense SAL around 4 km in altitude on 15 September 2022 (Fig. A5b) even when considering a larger geolocation offset from the Polly^{XT} (i.e. ≈ 350 km, instead of ≈ 13 km for 9 September 2022 and ≈ 20 km for 16 September 2022). Figures 4b–c, A4b–c, and A5b–c illustrate how the HALO 355 nm converted signals, even with low errors, may vary per Aeolus vertical range bin. This results in variabilities when re-gridding onto the Aeolus sampling, and it is a limitation of the cross-section comparison. Another limitation is illustrated with the offset between HALO and Polly^{XT} 355 nm converted signals, as it reveals uncertainties from the wavelength conversion.

Table 1. Summary of the statistics of the linear regression Aeolus MLEsub $\beta_{\text{part}}^{\parallel}$, MLEsub α_{part}, and SCA $\beta_{\text{part}}^{\text{att}\parallel}$ versus HALO 355 nm converted and re-gridded signals. The scores are derived from the log-transformed signals.

		9 Sep.	15 Sep.	16 Sep.
$\beta_{\text{part}}^{\parallel}$	R^2	0.69	0.56	0.60
	Slope	0.89	0.71	0.82
	RMSE	0.59	0.59	0.64
α_{part}	R^2	0.41	0.58	0.25
	Slope	1.08	1.09	0.71
	RMSE	0.68	0.66	0.73
$\beta_{\text{part}}^{\text{att}\parallel}$	R^2	0.48	0.28	0.14
	Slope	0.39	0.29	0.23
	RMSE	0.77	0.79	0.97

5.2 Cross-comparison of tropospheric sections observed by Aeolus ALADIN and DC-8 HALO

A linear regression has been applied with the log-transformed signals. Working with the logarithmic scale helps decrease the sensitivity to outliers that may be expected in low-SNR regions. Moreover, it offers a better visualization of regimes within two-dimensional histograms. The three indicators R^2, slope of the regression line, and root mean square error (RMSE) have been calculated with the log-transformed signals for each collocated section. Table 1 summarizes the scores. The R^2 values for the MLEsub backscatter $\beta_{\text{part}}^{\parallel}$ and MLEsub extinction α_{part} are robust, i.e. respectively up to 0.69 and 0.58, showing good agreement with the HALO retrievals. Interestingly, the higher R^2 scores correspond to 9 September 2022 for both MLEsub backscatter and SCA particulate attenuated backscatter $\beta_{\text{part}}^{\text{att}\parallel}$, the 15 September 2022 case showing the higher R^2 for MLEsub extinc-

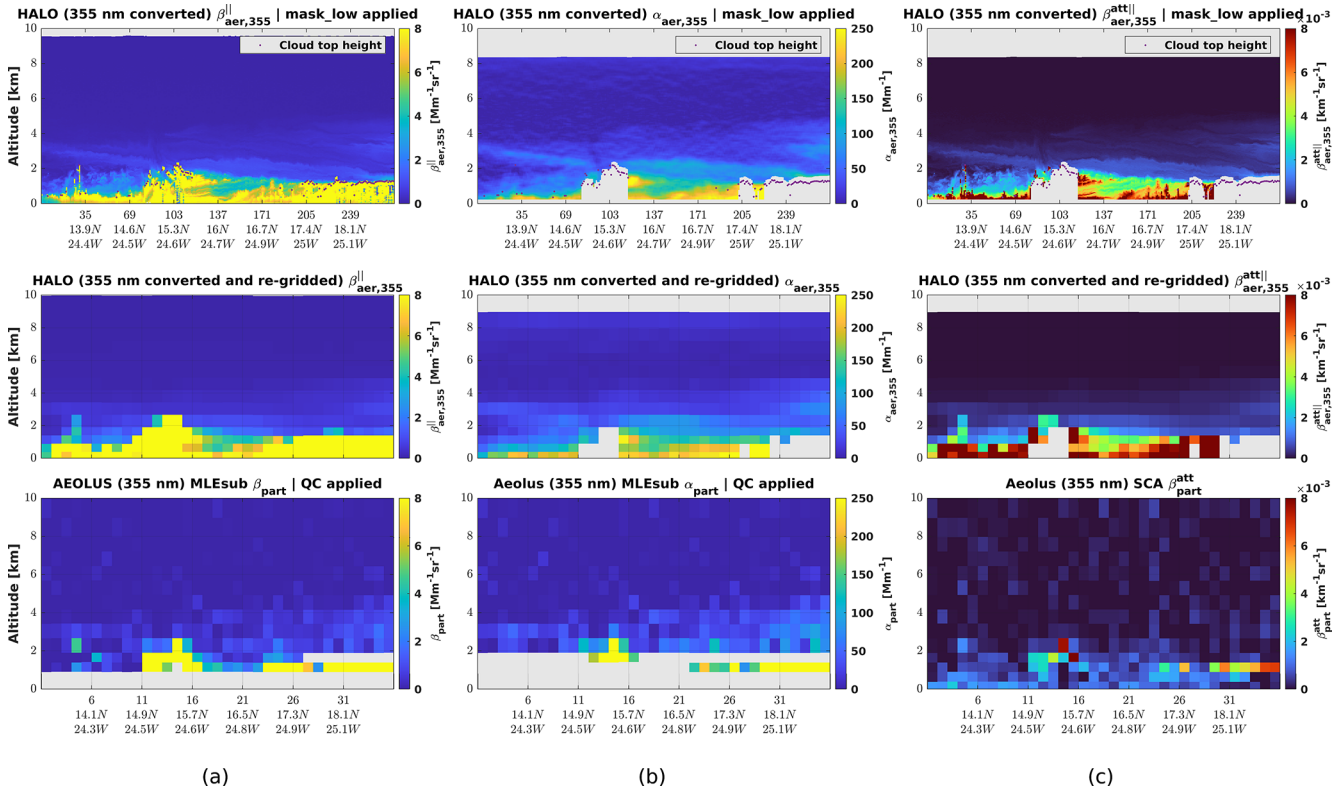

Figure 5. Aeolus MLEsub β_{part} **(a)**, MLEsub α_{part} **(b)**, and SCA $\beta^{\text{att}}_{\text{part}}$ **(c)** cross section collocated with HALO 355 nm converted products on 9 September 2022.

tion. For each scene, the section details are introduced before analysing the cross-comparison between HALO converted and re-gridded signals and the Aeolus products.

5.2.1 Case study: 9 September 2022

Cross section details. Figure 5a–c show HALO 355 nm converted (top) and re-gridded (middle) as well as Aeolus 355 nm (bottom) aerosol retrievals for a collocated section ≈ 626 km in the horizontal direction from $\approx$ [13.3° N–24.3° W] to $\approx$ [18.8° N–25.3° W]. A total of 271 HALO profiles can be re-gridded onto the 35 collocated Aeolus measurements. The geolocation offset for the first collocated measurement is equal to ≈ 5.2 km, and the initial time offset is equal to ≈ 9 min.

HALO against Aeolus MLEsub. HALO cloud_top_height superimposed over parallel 355 nm converted particulate backscatter revealed a marine boundary layer (MBL) up to ≈ 1 km in altitude with values above 8.0 $\text{Mm}^{-1}\,\text{sr}^{-1}$ (Fig. 5a top, light yellow). Low-altitude clouds are dominant close to the HALO profile ≈ 103 [15.3° N–24.6° W] and the last tier of the section above the HALO profile ≈ 205 [17.4° N–25.0° W]. Stratified marine and dusty mix aerosol layers can be seen up to ≈ 4 km in altitude, with backscatter from ≈ 3.0 to 5.0 $\text{Mm}^{-1}\,\text{sr}^{-1}$ (Fig. 5a, light blue to green), as confirmed with the HALO dominant aerosol type (see Fig. A1). Aeolus captures well the scene, even when applying the restrictive quality flags, which remove the lowest range bin below 1 km in altitude except for the cloudy region below dust in the last tier of the orbit section. The signature of the dust particle mixture can indeed be observed on top of the MBL (Fig. 5b bottom, light blue to green pattern with extinction close to $\approx 150\,\text{Mm}^{-1}$). The signature of the dust layer at ≈ 3 km in altitude close to the second-to-last Aeolus measurement 29 is even more clear. The Aeolus extinction is also flagged below the dusty mix around ≈ 1.8 km in altitude. This is a confirmation of a signal attenuation with low SNR.

The Aeolus backscatter (Fig. 5a bottom) appears lower for cloud top echoes when compared to the HALO 355 nm converted product before re-gridding (Fig. 5a top). For example, the HALO backscatter reaches values above 8.0 $\text{Mm}^{-1}\,\text{sr}^{-1}$ (Fig. 5a top, light yellow) for a localized cloud at ≈ 2 km in altitude for HALO profile 30 [13.8° N–24.3° W], and Aeolus-reported backscatter is $\approx 4.6\,\text{Mm}^{-1}\,\text{sr}^{-1}$ (Fig. 5a bottom, light green) for Aeolus measurement 4 at a similar altitude of ≈ 2 km. This confirms that Aeolus signal averaging with scattered or broken clouds may result in cloud echo dilution when the range bin encompasses the contribution of the lower backscatter signal from the surroundings. The averaging dilution is expected to be more pronounced with lower vertical resolution, i.e. with a thicker range bin, and with a

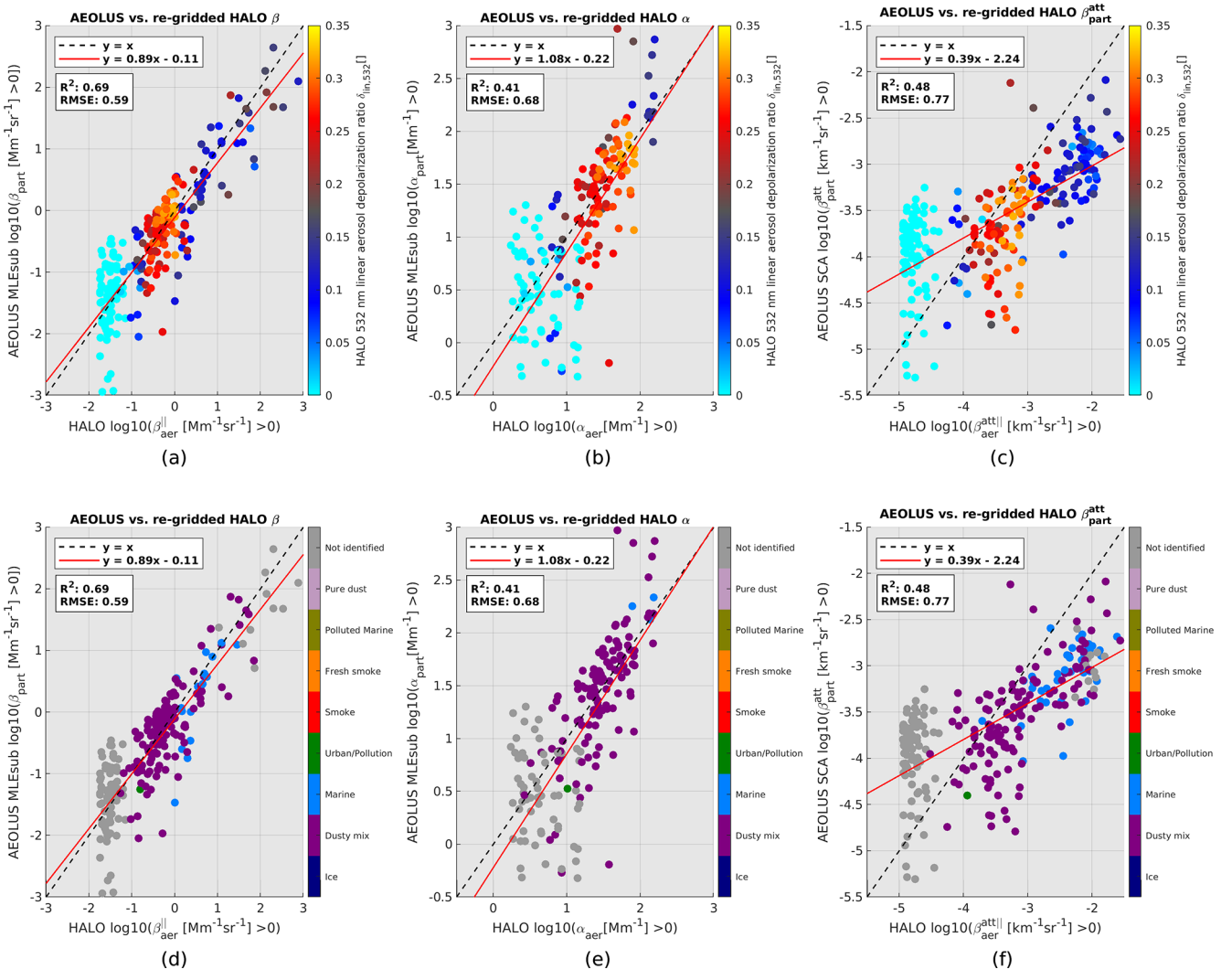

Figure 6. Two-dimensional histograms of Aeolus versus HALO 355 nm converted and re-gridded products with HALO $\delta_{\mathrm{circ},532}$ shown by varying colours **(a–c)** and with the HALO dominant aerosol type shown by varying colours **(d–f)** on 9 September 2022. A logarithmic transformation has been applied to the signals.

coarser horizontal resolution of ≈ 90 km for BRC level products.

Plotting the 355 nm converted and re-gridded HALO against Aeolus MLEsub for the whole scene reveals R^2 scores of 0.69 for backscatter (Fig. 6a) and 0.41 for extinction (Fig. 6b) with respective slopes for the regression line of 0.89 and 1.08. The agreement between Aeolus and HALO then appears consistent. Two dominant regimes can be identified using the HALO 532 nm linear aerosol depolarization ratio $\delta_{\mathrm{lin},532}$. The first one is indicated in cyan and corresponds to the low backscatter signal (Fig. 6a), with the HALO total scattering ratio at 532 nm R_{532} below a threshold of 1.2, which is required for HALO aerosol classification, hence the "Not identified" type (Fig. 6d, grey). The second regime comes with a dominant red-orange colour, with $\delta_{\mathrm{lin},532}$ above ≈ 0.25 (Fig. 6a–b), mainly attributed to dusty conditions (Freudenthaler et al., 2009). This is confirmed with a dusty mix class from HALO dominant aerosol type classification (Fig. 6d, dark violet). The HALO 532 nm circular aerosol depolarization ratio $\delta_{\mathrm{circ},532}$ shows values above ≈ 0.35 for this regime. The best agreement coincides with the second regime connected to highly depolarizing particles. The use of the HALO total scattering ratio at 532 nm R_{532} confirms that the first regime corresponds to low scattering (see Fig. A6, cyan). This provides further evidence that the first regime is linked to low-SNR regions of the atmosphere in clear sky conditions.

HALO against Aeolus SCA. Evidence of the MBL is visible with SCA particulate attenuated backscatter $\beta_{\mathrm{part}}^{\mathrm{att}}$ (Fig. 5c, bottom), and the values look coherent even for the low range bins (i.e. up to $\approx 3.0 \times 10^{-3}$ km^{-1} sr^{-1}). The top of the MBL is captured for the overall section. The SCA

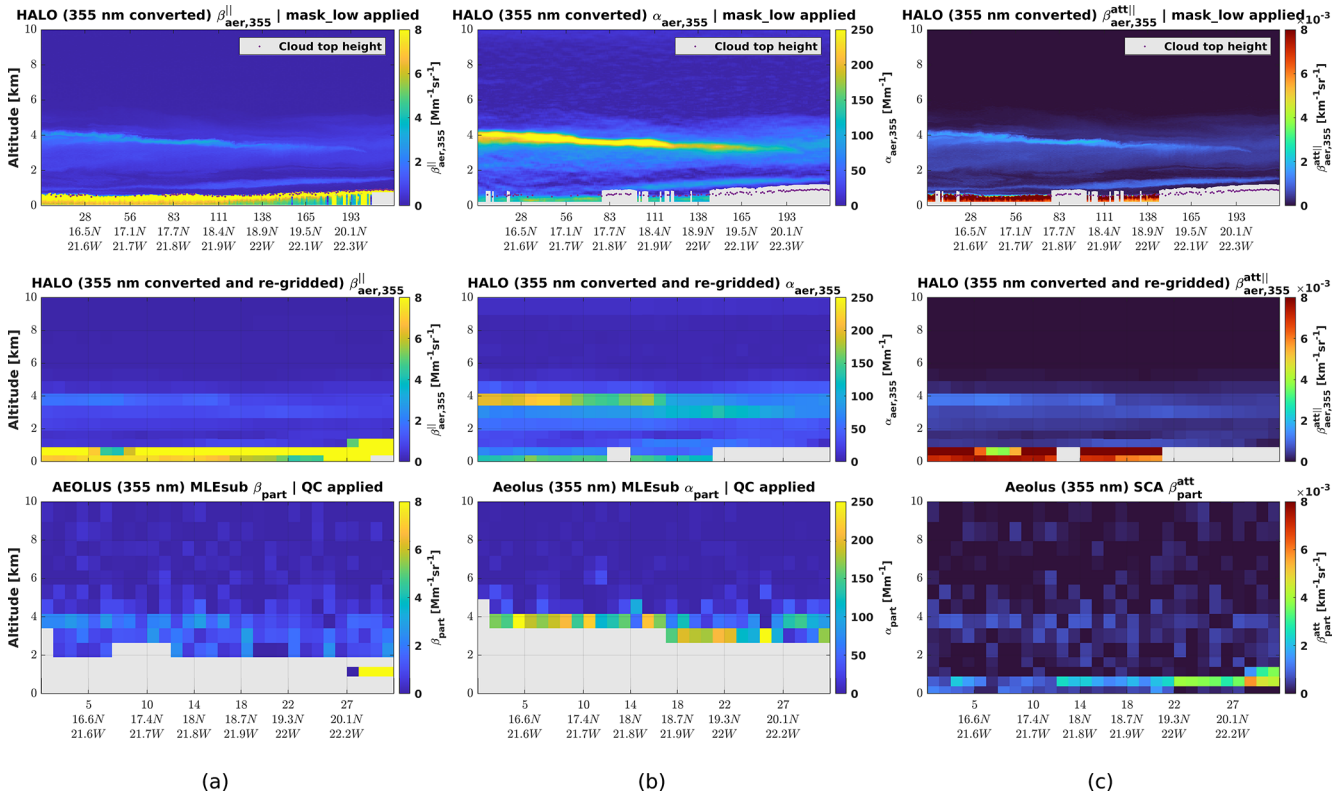

Figure 7. Aeolus MLEsub β_{part} **(a)**, MLEsub α_{part} **(b)**, and SCA $\beta^{\text{att}}_{\text{part}}$ **(c)** cross section collocated with HALO 355 nm converted products on 15 September 2022.

$\beta^{\text{att}}_{\text{part}}$ shows values below $\approx 2.0 \times 10^{-3}$ km^{-1} sr^{-1} for the dust above ≈ 2 km (Fig. 5c, light blue), which is hardly distinguishable from the background noise in the last tier of the orbit. When compared to the HALO 355 nm converted signal, these SCA $\beta^{\text{att}}_{\text{part}}$ values look underestimated. The scatter diagram confirms an underestimation of the SCA particulate attenuated backscatter for the second regime. The SCA seems to overestimate the backscatter for the first regime in low scattering regions of the atmosphere (Fig. A7, cyan). When removing this regime from the analysis using HALO R_{532} and applying a threshold of 1.2, R^2 increases from 0.48 to 0.52, and RMSE decreases from 0.77 to 0.70. A positive impact is also observed for MLEsub backscatter (i.e. R^2 increasing from 0.69 to 0.71 and RMSE decreasing from 0.59 to 0.43) and extinction (i.e. R^2 increasing from 0.41 to 0.47 and RMSE decreasing from 0.68 to 0.38). Interestingly, a third regime in high backscatter regions can be identified, with $\delta_{\text{lin},532}$ from ≈ 0.05 to ≈ 0.10 (Fig. 6c, dark blue) and $\delta_{\text{circ},532}$ reaching values of ≈ 0.10 to ≈ 0.20. The HALO dominant aerosol type points to a mixture of marine aerosols and dusty mix (Fig. 6f, blue and dark violet). The SCA appears to underestimate the signal for this regime, which includes marine aerosols.

5.2.2 Case study: 15 September 2022

Cross section details. Figure 7a–c show HALO 355 nm converted (top) and re-gridded (middle) as well as Aeolus 355 nm (bottom) aerosol retrievals for a collocated section ≈ 537 km in the horizontal direction from $\approx$ [15.9° N–21.5° W] to $\approx$ [20.7° N–22.4° W]. A total of 218 HALO profiles can be re-gridded onto 30 collocated Aeolus measurements. The geolocation offset for the first collocated measurement is equal to ≈ 3.8 km, and the initial time offset is equal to ≈ 13 min.

HALO against Aeolus MLEsub. HALO cloud_top_height superimposed over parallel 355 nm converted particulate backscatter shows optically dense MBL up to 0.5 km in altitude (Fig. 7a, top). A homogeneous feature, spatially distributed over the scene, with backscatter up to ≈ 5.0 Mm^{-1} sr^{-1}, can be observed around 4 km in altitude (light green to yellow), which is typical for the SAL height (Ansmann et al., 2009). The HALO dominant aerosol type confirms the presence of dusty mix (see Fig. A2). The SAL is clearly captured by the MLEsub algorithm, the southern edge of the aerosol layer being particularly visible up to Aeolus measurement 18 [18.7° N–21.9° W] with both MLEsub backscatter and extinction coefficients (Fig. 7a–b). The MLEsub products are flagged below this dense and homoge-

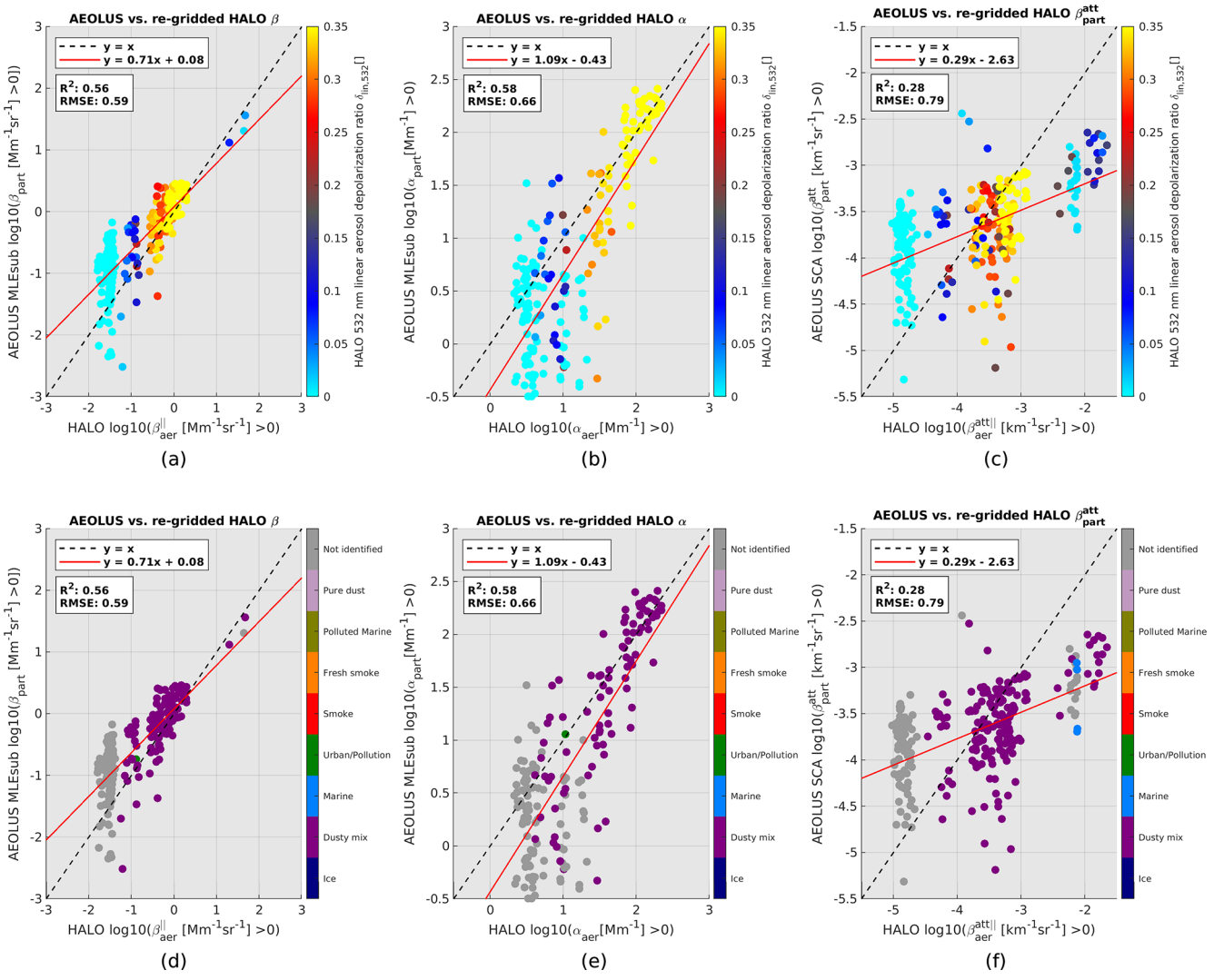

Figure 8. Two-dimensional histograms of Aeolus versus HALO 355 nm converted and re-gridded products with HALO $\delta_{\mathrm{circ},532}$ shown by varying colours **(a–c)** and with the HALO dominant aerosol type shown by varying colours **(d–f)** on 15 September 2022. A logarithmic transformation has been applied to the signals.

neous aerosol layer. The backscatter scatter diagram shows robust agreement between Aeolus and HALO for the dusty mix regime (dark violet colour in Fig. 8d), with an R^2 score of 0.56. This regime corresponds to a HALO $\delta_{\mathrm{lin},532}$ above ≈ 0.25 (Fig. 8a, red-orange to yellow) and HALO $\delta_{\mathrm{circ},532}$ above ≈ 0.35. The main deviations correspond to the first regime, where aerosol loading is weak and falls below the classification threshold of 1.2 in the HALO total scattering ratio at 532 nm R_{532}.

HALO against Aeolus SCA. The Aeolus SCA is able to capture well the dusty mix layer at ≈ 4 km (Fig. 7c bottom, light blue) and the MBL below ≈ 0.8 km. Values of particulate attenuated backscatter up to $\approx 8.0 \times 10^{-4}$ km^{-1} sr^{-1} are measured for the southern edge of the aerosol layer close to Aeolus measurement 5 [16.6° N–21.6° W]. The aerosol layer signature is less clear in the last tier of the scene, i.e. after Aeolus measurement 18 [18.7° N–21.9° W] with SCA $\beta^{\mathrm{att}}_{\mathrm{part}}$ below $\approx 2.0 \times 10^{-4}$ km^{-1} sr^{-1}. This may be used as a first estimation for the lower limit of SCA $\beta^{\mathrm{att}}_{\mathrm{part}}$ detection for dust particles. The scatter diagram shows an R^2 score of 0.28, and the higher deviations are once more observed for low scattering (see Fig. A7). The better agreement is observed for the dusty mix regime (red-orange to yellow in Fig. 8c). Removing the contributions from low scattering below HALO R_{532} of 1.2 has a significant impact on the slope (i.e. increased from 0.29 to 0.40).

5.2.3 Case study: 16 September 2022

Cross section details. Figure 9a–c show HALO 355 nm converted (top) and re-gridded (middle) as well as Aeolus 355 nm (bottom) aerosol retrievals for a collocated sec-

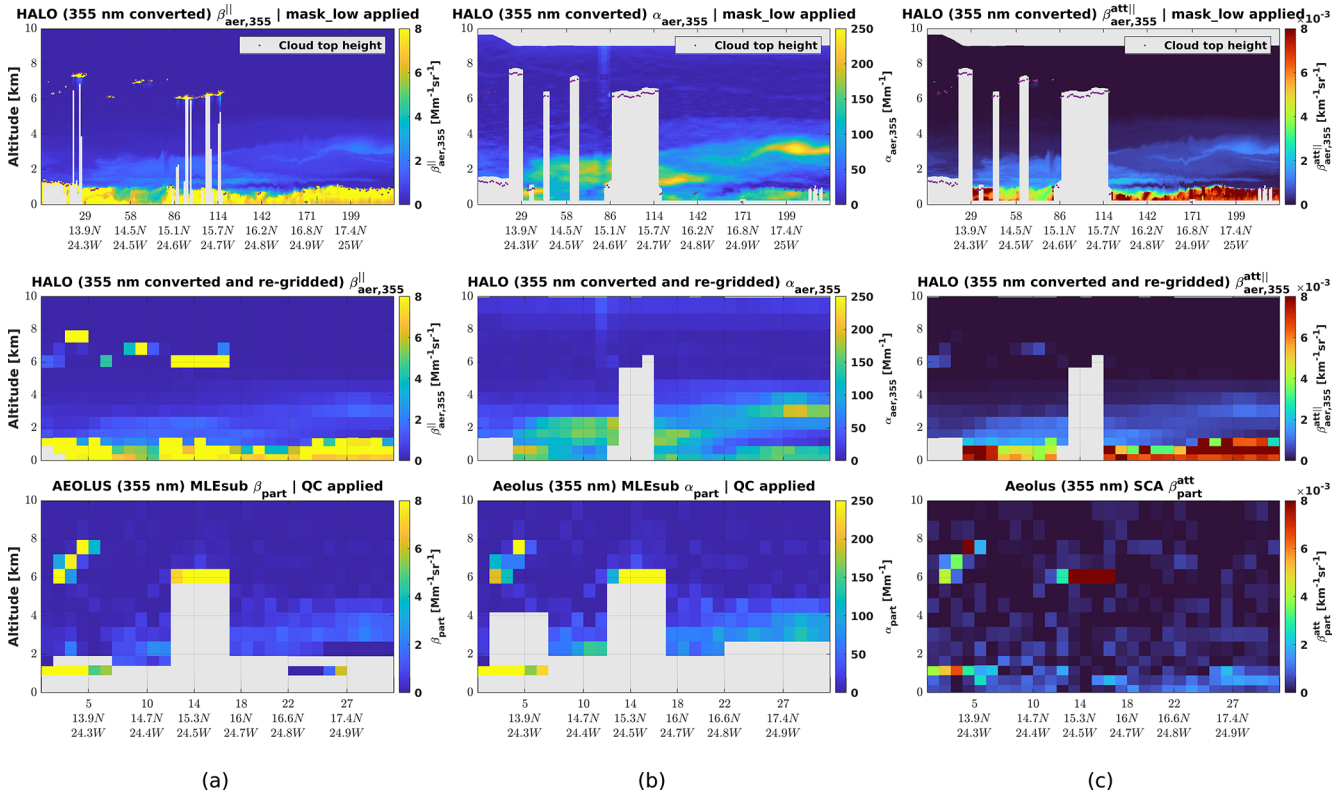

Figure 9. Aeolus MLEsub β_{part} **(a)**, MLEsub α_{part} **(b)**, and SCA $\beta^{\text{att}}_{\text{part}}$ **(c)** cross section collocated with HALO 355 nm converted products on 16 September 2022.

tion ≈ 538 km in the horizontal direction from ≈ [13.2° N–24.3° W] to ≈ [17.9° N–25.1° W]. A total of 225 HALO profiles can be re-gridded onto 30 collocated Aeolus measurements. The geolocation offset for the first collocated measurement is equal to ≈ 2 km, and the initial time offset is equal to ≈ 25 min.

HALO against Aeolus MLEsub. HALO cloud_top_height superimposed over parallel 355 nm converted particulate backscatter reveals some broken clouds at ≈ 6 km in altitude in the first tier of the tropospheric section. Two main stratified features with strong signatures are particularly noticeable. They are distributed between HALO profiles 29 [13.9° N–24.3° W] and 142 [16.2° N–24.8° W] at ≈ 2 km in altitude and within the last tier of the section by HALO profile ≈ 171 [16.8° N–24.9° W] at ≈ 3 km in altitude. The HALO dominant aerosol type mainly classifies the two layers as pure dust (see Fig. A3). Aeolus captures well the two dust layers. They are particularly visible with the Aeolus MLEsub extinction coefficient (Fig. 9b bottom, light blue to green). A decrease in HALO 355 nm converted extinction can be observed at the top altitude close to HALO profile 86 [15.1° N–24.6° W].

The backscatter scatter diagram reveals good agreement between HALO and Aeolus, with R^2 of 0.60. The best agreement corresponds to the non-spherical particles regime classified as dusty mix by the HALO dominant aerosol type product (i.e. dark violet colour in Fig. 10d). HALO and Aeolus are in very good agreement for the core dust layer (i.e. red-orange point clouds close to the $y = x$ line for Fig. 10a–b), classified as pure dust with the HALO classification (Fig. 10d–e, rose colour). HALO $\delta_{\text{lin},532}$ reaches ≈ 0.30 for such a layer that is indeed pointing to dust conditions (Freudenthaler et al., 2009; Haarig et al., 2017a, 2022). HALO $\delta_{\text{circ},532}$ shows values up to ≈ 0.40 for this pure dust regime. The ability of Aeolus to achieve physical retrievals even for highly depolarizing particles such as SAL is then demonstrated. The larger outliers cannot be attributed to an aerosol type and are distributed in aerosol-free regions with low and high backscatter (Fig. 10d, grey). This may point to a low signal and bins contaminated by clouds. The scene indeed includes dense clouds close to ≈ 6 km in altitude (Fig. 9a). One could flag the cloudy regions by applying a scattering ratio threshold of 5 (Chepfer et al., 2013; Feofilov et al., 2022). If combined with the low scattering removal (i.e. $1.2 < R_{532} <= 5$), this has a positive impact (e.g. decrease in RMSE from 0.64 to 0.38 for the MLEsub backscatter and from 0.73 to 0.41 for the MLEsub extinction).

HALO against Aeolus SCA. The SCA underestimates the signal from the marine aerosol regime (Fig. 10f, blue). Both HALO and SCA reveal broken clouds around ≈ 6 to ≈ 8 km for the first half of the orbit, and the signature of the pure dust

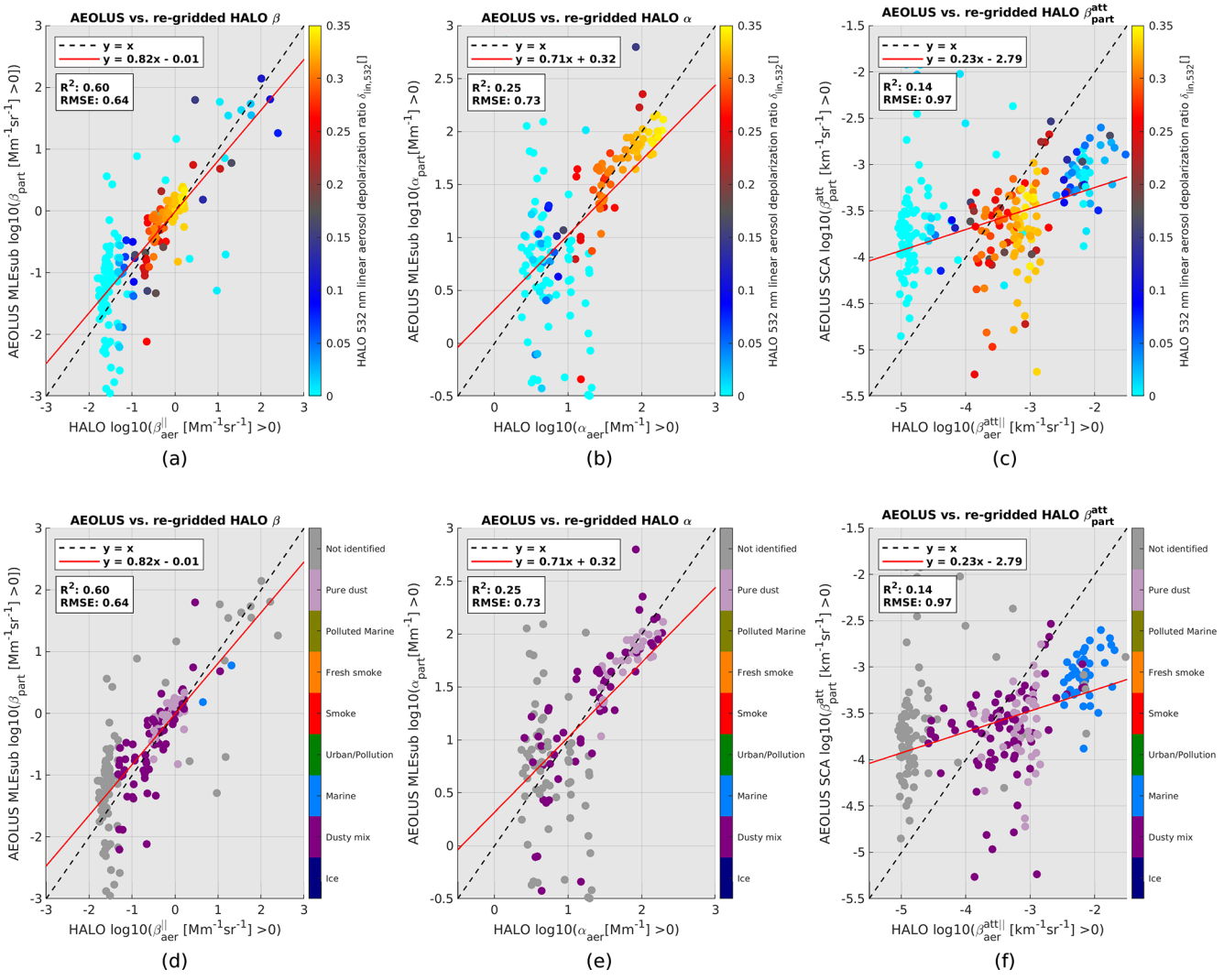

Figure 10. Two-dimensional histograms of Aeolus versus HALO 355 nm converted and re-gridded products with HALO $\delta_{\mathrm{circ},532}$ shown by varying colours **(a–c)** and with the HALO dominant aerosol type shown by varying colours **(d–f)** on 16 September 2022. A logarithmic transformation has been applied to the signals.

layer close to the second-to-last Aeolus measurement 29 is observable within the SCA particulate attenuated backscatter (Fig. 9c, bottom, light blue). The scatter diagram shows an R^2 score of 0.14, and the best agreement is observed for the pure dust and dusty mix regimes (dark violet and rose colours in Fig. 10f), despite some outliers. The lowest correlation once more corresponds to low-signal regions of the atmosphere (Fig. 10f, grey) with low scattering (Fig. A8c, cyan), for which the SCA appears to overestimate the particulate attenuated backscatter.

6 Conclusion

The study presents three cross sections of the atmosphere above the tropical Atlantic as observed by the ALADIN instrument on board the Aeolus satellite and reference lidar systems. For the first time, Aeolus aerosol observing capabilities are evaluated with extended tropospheric sections up to 626 km in length with a small geolocation offset (i.e. less than 6 km) and time offset (i.e. less than 30 min). The Aeolus L2A aerosol products at 355 nm retrieved with the SCA and MLEsub algorithms have been compared to independent measurements from the HALO lidar on board NASA DC-8 aircraft, the 532 nm signal being converted to 355 nm and re-gridded onto Aeolus sampling. In addition, direct profiles above ground-based Raman lidar Polly$^{\mathrm{XT}}$ have been analysed.

Despite the different geometries (i.e. nadir-viewing angle for HALO, off-nadir $\approx 35°$ for Aeolus), good agreement between the aerosol retrievals is shown for homogeneous, optically thick aerosol layers. The cross-comparison of the

MLEsub backscatter and extinction coefficients for particles with HALO retrievals reveal R^2 scores up to 0.69 and 0.58, respectively. When looking at the particulate attenuated backscatter coefficient derived with SCA, the R^2 scores reach ≈ 0.48. A good agreement is observed for highly depolarizing aerosol layers classified as pure dust and dusty mix with the HALO dominant aerosol type product, and likewise for each scene on 9, 15, and 16 September 2022. Higher deviations are observed for aerosol-free regions of the atmosphere, where the SNR is expected to be very low. The study reveals that the agreement between the Aeolus and reference measurements can be improved when applying a scattering ratio threshold that complements the QC flags in order to focus on cloud-free regions of the atmosphere with high SNR and higher aerosol loads (e.g. flagging the bins out of a range of 1.2–5). This provides further evidence that the SNR and an adequate cloud screening approach are important parameters to consider when using the Aeolus L2A product for aerosol profiling.

Optical characteristics of marine aerosols and clouds below a dust mixture are well captured by Aeolus (e.g. 9 September 2022), suggesting that the UV laser emissions can penetrate enough of the aerosol layer distributed in irregular-shaped particles with a linear aerosol depolarization ratio at 532 nm above 0.25. The opposite condition, i.e. a diffuse aerosol layer below broken clouds, should be analysed with caution, as the low SNR seems insufficient to trust retrievals of a low backscatter coefficient (e.g. 16 September 2022). The spatial extent of aerosol layers such as SAL is clearly visible with L2A MLEsub, as the optimal estimation approach helps to smooth the signal over consecutive profiles (i.e. the SCA standard concept corresponds to an along-track averaging of the lidar signal, resulting in high noise dependency). We then recommend opting for the MLEsub dataset if focusing on long and homogeneous layers. The SCA retrievals appear noisier, showing higher sensitivity to signal attenuation in low scattering regions of the atmosphere. The SCA also underestimates the particulate attenuated backscatter for both dusty mix and marine regimes. The Aeolus RBS and their in-orbit deviations must be considered with caution, as better optical properties would be obtained when the range bins do not encompass layer edges or complex mixture. We then recommend focusing on settings below a 1 km thickness when studying vertical sedimentation of ageing thin layers. Moreover, the Aeolus signal from scattered or broken clouds should be analysed with caution, as cloud echo dilution can be observed when signal averaging includes the contribution from the surroundings with a lower backscatter signal. The averaging dilution is expected to be more prominent, with a coarser horizontal resolution BRC ≈ 90 km. We then recommend using the sub-BRC level products when focusing on signals from localized clouds. One should note the negative impact of low SNR below an altitude of 2 km, where the MLEsub products appear to be flagged by the QC and where the range bin thickness decreases from 750 to 500 m for the Cabo Verde region.

The present study demonstrates the independent HSRL measurement of aerosol properties such as particle extinction and backscatter coefficients, even for missions initially designed for winds, such as Aeolus. The collocation of the Aeolus data with the HALO polarization measurements demonstrates the aerosol typing capabilities and provides further evidence of the need for Aeolus-2 to have polarization capabilities. The Aeolus MLEsub extinction is recommended for aerosol layer detection, and both the MLEsub backscatter and SCA particulate attenuated backscatter allow capturing water clouds with strong signals below dusty mix. The study illustrates how Aeolus is capable of measuring the optical properties of aerosols, even for highly depolarizing particles once correcting the missing cross-polarized signal. This provides support for further development of a new Aeolus product (e.g. co-polarized to the total backscatter coefficient using depolarization information from another instrument). The validation of the Aeolus L2A SCA and MLEsub products with extended and collocated tropospheric sections with high-spectral-resolution lidar also supports the first estimation of the lower limits for backscatter detection (e.g. $\approx 1.0 \times 10^{-7}\,\mathrm{m^{-1}\,sr^{-1}}$ for dusty mix, focusing on a quality-flagged MLEsub backscatter coefficient for particles, and $\approx 2.0 \times 10^{-4}\,\mathrm{km^{-1}\,sr^{-1}}$ for dust mix, focusing on SCA particulate attenuated backscatter). The use of the arithmetic mean when re-gridding independent measurements onto the Aeolus sampling is straightforward, but one could derive the confidence index as a function of the SNR, aerosol types detected with ad hoc classification, or portion of the valid measurements considered per Aeolus coarser range bin. Vertical sampling is a limitation to bear in mind for new missions such as EarthCARE and Aeolus-2; the finer the vertical resolution with a strong signal, the better the measurement will allow analysis of a diffuse aerosol plume and mixture where complex atmospheric processes occur. The importance of a polarization channel for the next generation of instrument is also demonstrated, as it enables aerosol typing, which now becomes a major objective for aerosol missions. Finally, it would be beneficial to reproduce the validation of the Aeolus L2A product with independent lidar measurements focusing on the early mission period, as a significant signal loss was reported for the ALADIN instrument throughout the satellite lifetime (Lux et al., 2024; Reitebuch et al., 2024). One would expect a higher signal and better performance of the L2A algorithms than for the period of September 2022 selected for this paper. The public release of the Aeolus reprocessed dataset, labelled Baseline 16 and covering 2018 to 2019, is planned for 2025 and can be used for the study.

Appendix A

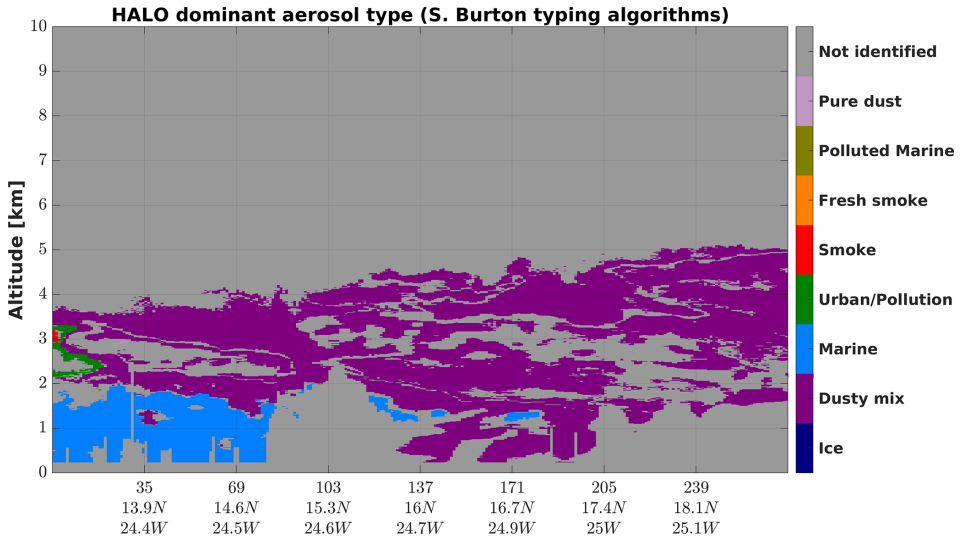

Figure A1. HALO 532 nm dominant aerosol type for 9 September 2022, with aerosol-free regions marked as "Not identified".

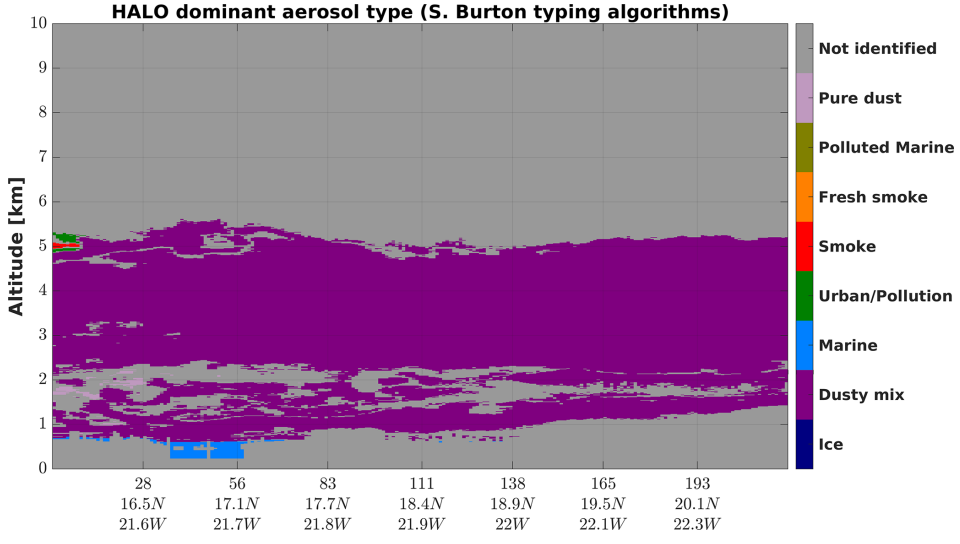

Figure A2. HALO 532 nm dominant aerosol type for 15 September 2022, with aerosol-free regions marked as "Not identified".

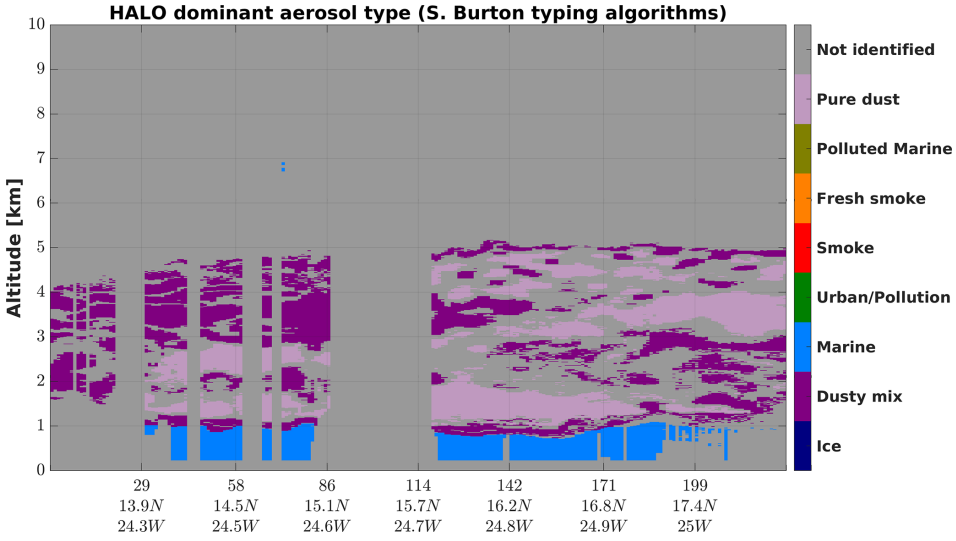

Figure A3. HALO 532 nm dominant aerosol type for 16 September 2022, with aerosol-free regions marked as "Not identified".

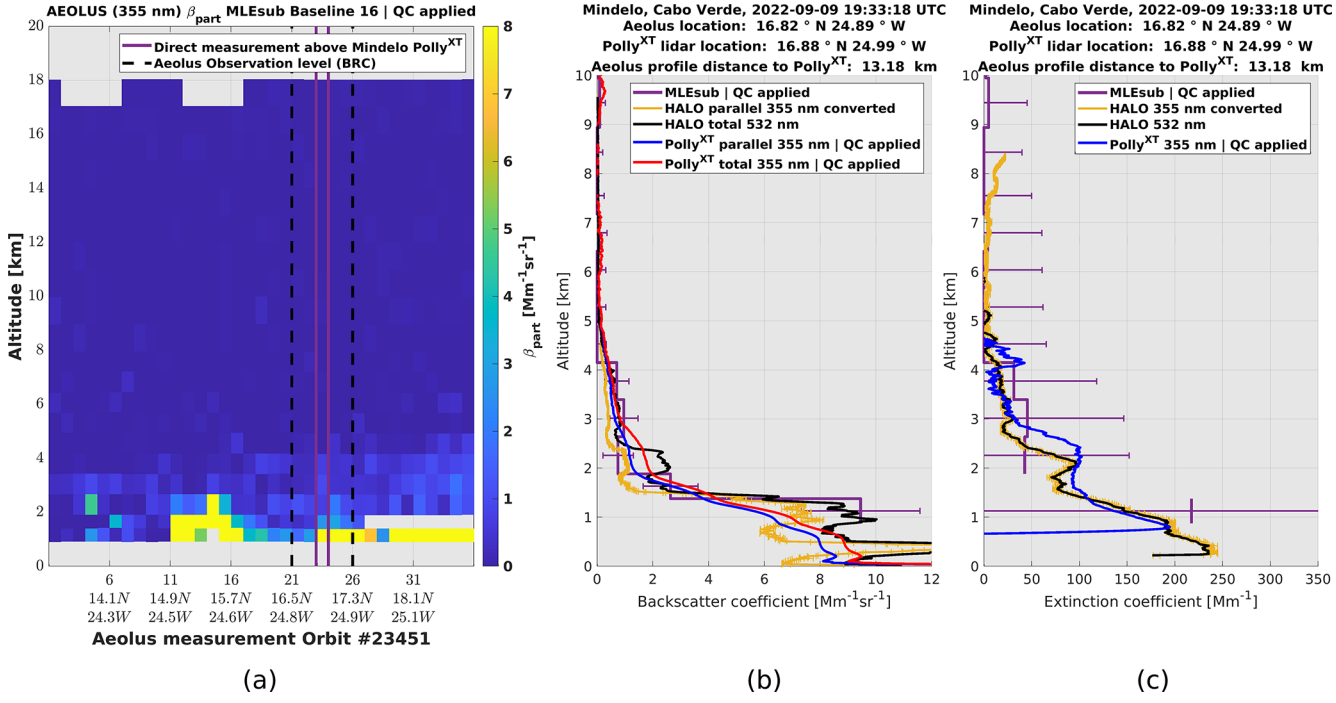

Figure A4. Aeolus MLEsub β_{part} on 9 September 2022 **(a)** and cross-comparison of 2D profiles above Mindelo, Cabo Verde, with HALO and Polly$^{\text{XT}}$ for MLEsub β_{part} **(b)** and MLEsub α_{part} **(c)**.

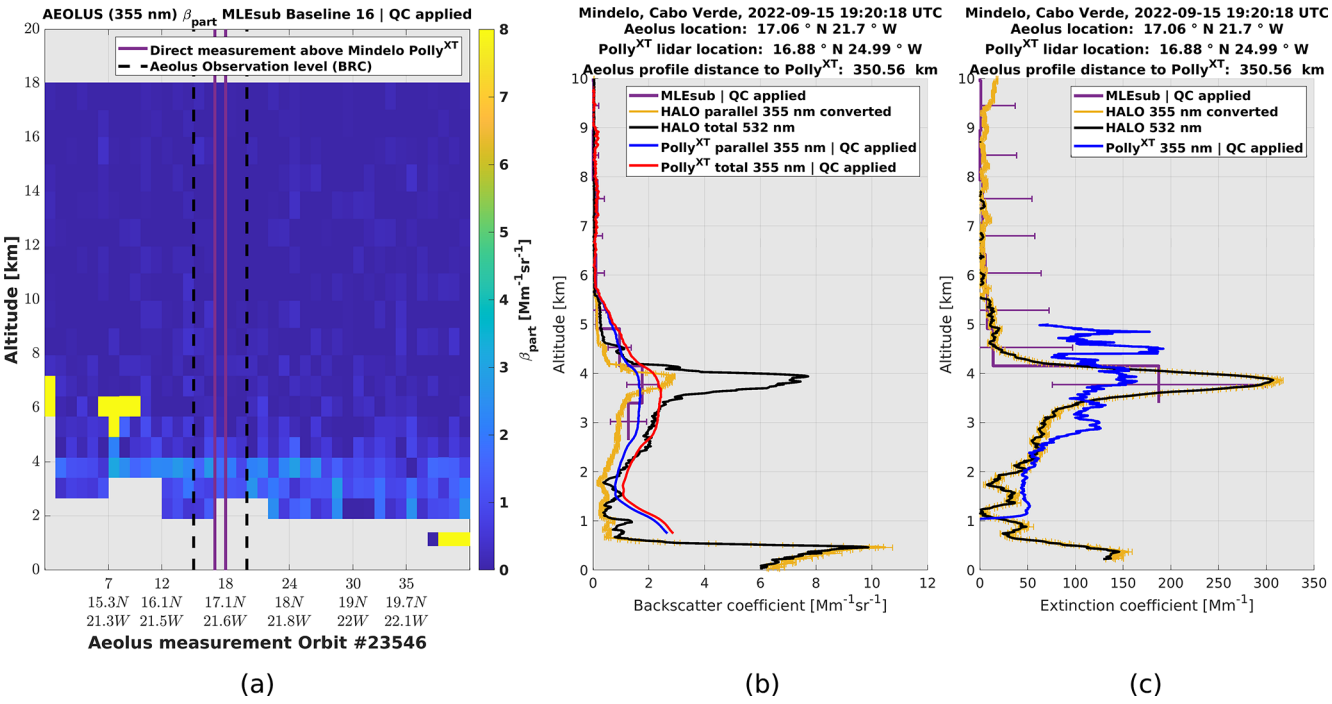

Figure A5. Aeolus MLEsub β_{part} on 15 September 2022 **(a)** and cross-comparison of 2D profiles above Mindelo, Cabo Verde, with HALO and Polly$^{\text{XT}}$ for MLEsub β_{part} **(b)** and MLEsub α_{part} **(c)**.

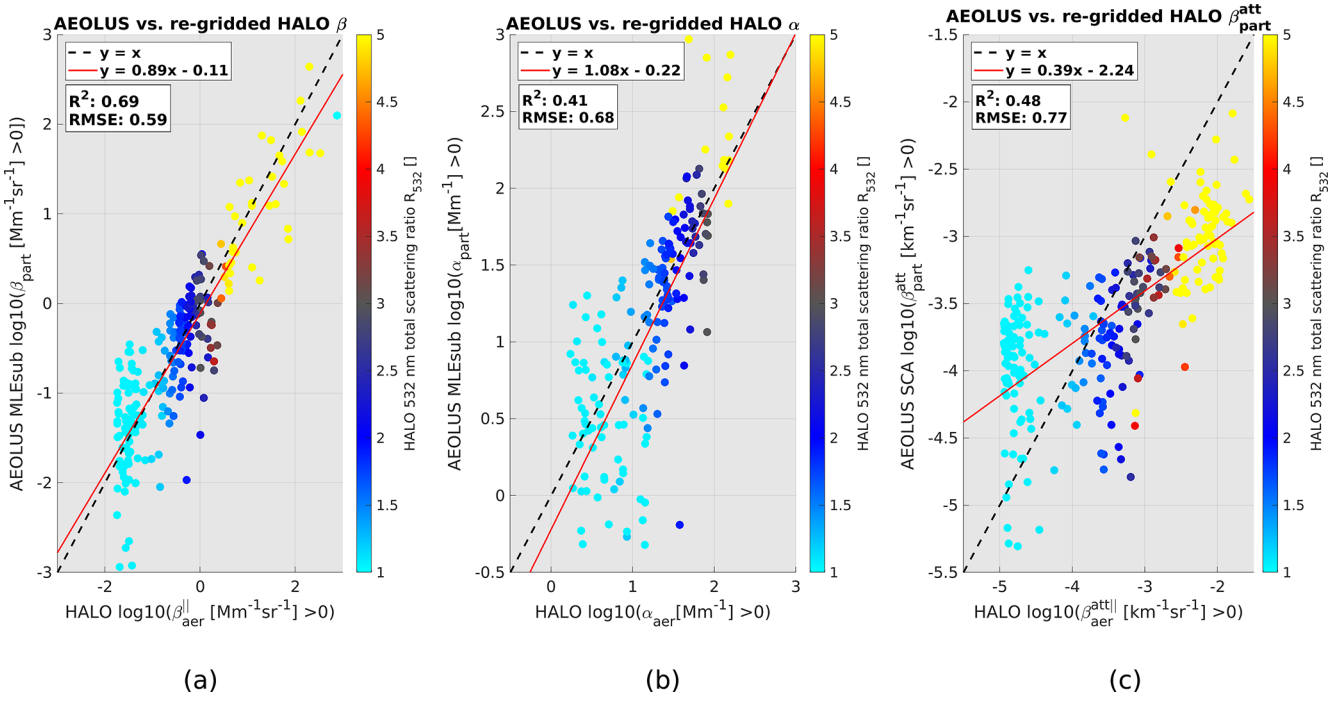

Figure A6. Two-dimensional histograms of Aeolus MLEsub β_{part} **(a)**, MLEsub α_{part} **(b)**, and SCA $\beta^{\text{att}}_{\text{part}}$ **(c)** versus HALO 355 nm converted and re-gridded products with HALO R_{532} shown by varying colours on 9 September 2022.

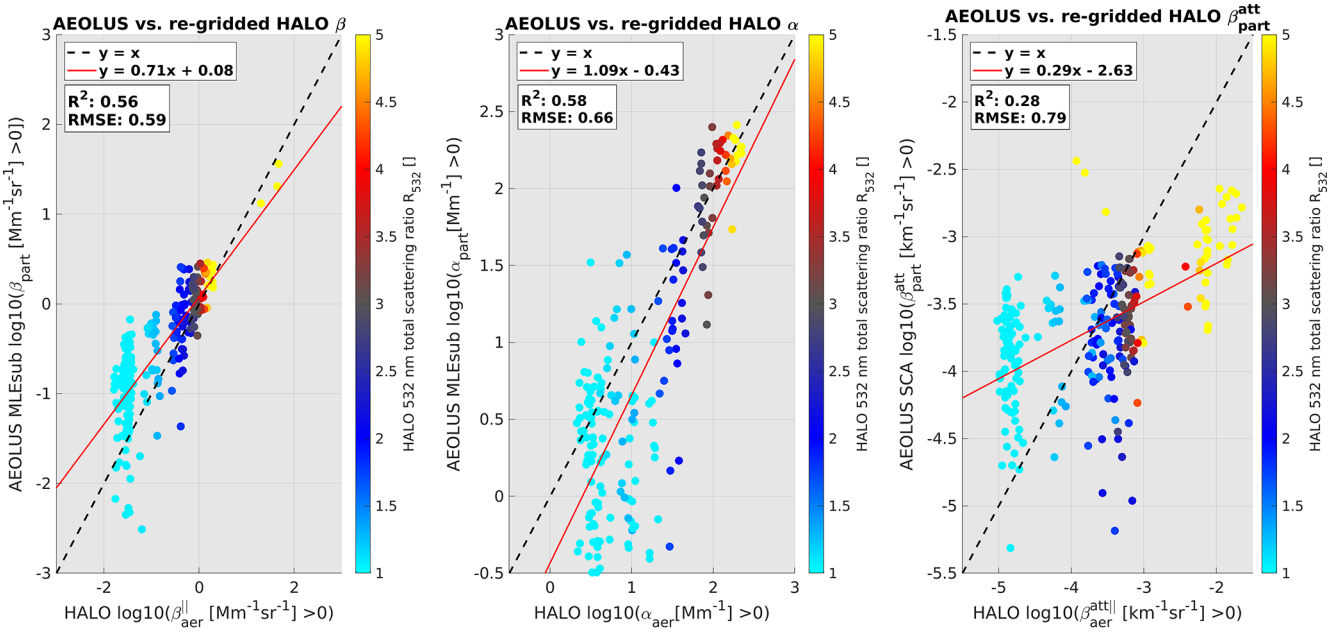

Figure A7. Two-dimensional histograms of Aeolus MLEsub β_{part} **(a)**, MLEsub α_{part} **(b)**, and SCA $\beta_{\text{part}}^{\text{att}}$ **(c)** versus HALO 355 nm converted and re-gridded products with HALO R_{532} shown by varying colours on 15 September 2022.

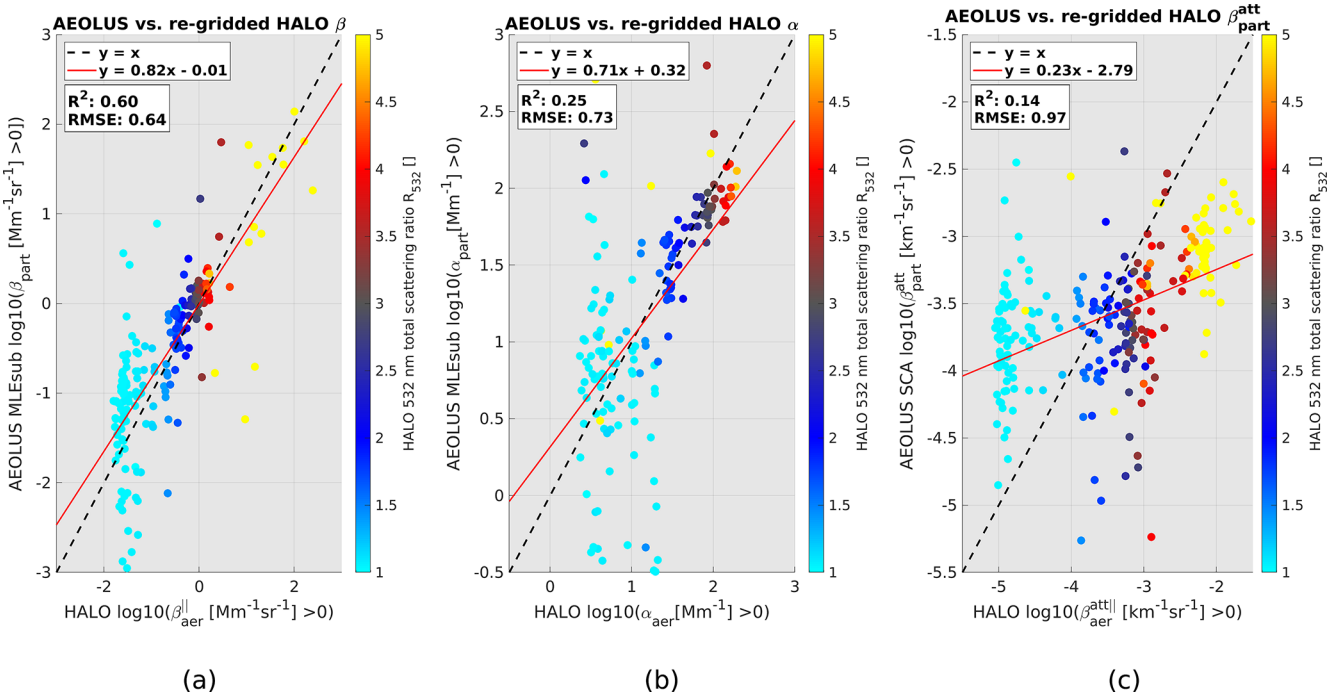

Figure A8. Two-dimensional histograms of Aeolus MLEsub β_{part} **(a)**, MLEsub α_{part} **(b)**, and SCA $\beta_{\text{part}}^{\text{att}}$ **(c)** versus HALO 355 nm converted and re-gridded products with HALO R_{532} shown by varying colours on 16 September 2022.

Code and data availability. The study includes Aeolus aerosol products prepared by the Aeolus DISC (involving ESA, DLR, DoRIT, ECMWF, KNMI, CNRS until 31 December 2022, TROPOS, S&T, ABB, and Serco) and the Payload Data Ground Segment (PDGS) through the reprocessing activities. The corresponding dataset of September 2022 is part of the fourth reprocessing, labelled Baseline 16 and covering July 2019 to April 2023. The first part of this dataset was released to the public on May 2024. The Aeolus L2A data have gradually been made public since May 2021 through the ESA Aeolus Online Dissemination System ADDF at http://aeolus-ds.eo.esa.int/oads/access/ (ESA, 2024). The Python plotting library Matplotlib (Hunter, 2007) has been used for the study as the bipolar colour map, which can be downloaded from the MATLAB Central File Exchange at https://www.mathworks.com/matlabcentral/fileexchange/26026-bipolar-colormap (Ridgway, 2025). The HALO DC-8 data have been downloaded from https://doi.org/10.5067/ASDC/SUBORBITAL/CPEXCV-HALO_DC8_1 (NASA/LARC/SD/ASDC, 2023). Data of JATAC/ASKOS 2021 and 2022 are publicly available via the ESA Validation Data Center (EVDC) data portal, available at https://doi.org/10.60621/jatac.campaign.2021.2022.caboverde (Amiridis et al., 2023).

Author contributions. The study was conducted in the frame of Aeolus-DISC as part of L2A processor version 16 development and validation activities. The contributors to the maintenance and improvement of the L2A SCA and MLE algorithms are DT (present), AL (former), TF (former), and AD (former). The operational version of the L2A processor was prepared by DH before deployment at ESA. AN is the principal investigation and technical point of contact for the data associated with the NASA HALO instrument. MH provided the estimations of the backscatter-related Ångström exponent and extinction-related Ångström exponent measured with the Polly^{XT} instrument. The paper was written by DT.

Competing interests. The contact author has declared that none of the authors has any competing interests.

Disclaimer. Publisher's note: Copernicus Publications remains neutral with regard to jurisdictional claims made in the text, published maps, institutional affiliations, or any other geographical representation in this paper. While Copernicus Publications makes every effort to include appropriate place names, the final responsibility lies with the authors.

Special issue statement. This article is part of the special issue "The Joint Aeolus Tropical Atlantic Campaign (JATAC) (AMT/ACP inter-journal SI)". It is not associated with a conference.

Acknowledgements. We thank all previous contributors to the L2A product development and validation from Météo-France CNRM/CNRS (Pierre Flamant, Marie-Laure Denneulin, Mathieu Olivier, Vincent Lever, Pauline Martinet, Hugo Stieglitz, and Ibrahim Seck). We acknowledge TROPOS members involved in the Ocean Science Centre Mindelo (OSCM) instrumentation maintenance (Ronny Engelmann, Dietrich Althausen, and Annet Skupin). We also acknowledge the HALO team for the collection of the CPEX-CV dataset, as well as the entire CPEX-CV science, instrument, and aircraft operations teams for the successful execution of the CPEX-CV campaign. We also thank Aaron Piña (United States Forest Service, USFS) and Edward P. Nowottnick (NASA Goddard Space Flight Center) for their support within JATAC. Finally, we acknowledge Oliver Reitebuch (German Aerospace Center DLR), who internally reviewed the present paper.

Review statement. This paper was edited by Eleni Marinou and reviewed by two anonymous referees.

References

Abril-Gago, J., Guerrero-Rascado, J. L., Costa, M. J., Bravo-Aranda, J. A., Sicard, M., Bermejo-Pantaleón, D., Bortoli, D., Granados-Muñoz, M. J., Rodríguez-Gómez, A., Muñoz-Porcar, C., Comerón, A., Ortiz-Amezcua, P., Salgueiro, V., Jiménez-Martín, M. M., and Alados-Arboledas, L.: Statistical validation of Aeolus L2A particle backscatter coefficient retrievals over ACTRIS/EARLINET stations on the Iberian Peninsula, Atmos. Chem. Phys., 22, 1425–1451, https://doi.org/10.5194/acp-22-1425-2022, 2022.

Amiridis, V., Marinou, E., Paschou, P., Baars, H., Pirloaga, R., Engelmann, R., Tsekeri, A., Daskalopoulou, V., Kazadzis, S., Skupin, A., Marenco, F., Kezoudi, M., Kouklaki, D., Siomos, N., Floutsi, A., Metallinos, S., Spanakis Misirlis, V., Raptis, P., Althausen, D., Seifert, P., Nemuc, A., Antonescu, B., Papetta, A., and Wandinger, U.: ASKOS Campaign Dataset, ESA Atmospheric Validation Data Centre [data set], https://doi.org/10.60621/jatac.campaign.2021.2022.caboverde, 2023.

Ansmann, A., Wagner, F., Müller, D., Althausen, D., Herber, A., von Hoyningen-Huene, W., and Wandinger, U.: European pollution outbreaks during ACE 2: Optical particle properties inferred from multiwavelength lidar and star-Sun photometry, J. Geophys. Res.-Atmos., 107, AAC 8–1–AAC 8–14, https://doi.org/10.1029/2001JD001109, 2002.

Ansmann, A., Tesche, M., Knippertz, P., Bierwirth, E., Althausen, D., Müller, D., and Schulz, O.: Vertical profiling of convective dust plumes in southern Morocco during SAMUM, Tellus B, 61, 340–353, https://doi.org/10.1111/j.1600-0889.2008.00384.x, 2009.

Baars, H., Kanitz, T., Engelmann, R., Althausen, D., Heese, B., Komppula, M., Preißler, J., Tesche, M., Ansmann, A., Wandinger, U., Lim, J.-H., Ahn, J. Y., Stachlewska, I. S., Amiridis, V., Marinou, E., Seifert, P., Hofer, J., Skupin, A., Schneider, F., Bohlmann, S., Foth, A., Bley, S., Pfüller, A., Giannakaki, E., Lihavainen, H., Viisanen, Y., Hooda, R. K., Pereira, S. N., Bortoli, D., Wagner, F., Mattis, I., Janicka, L., Markowicz, K. M., Achtert, P., Artaxo, P., Pauliquevis, T., Souza, R. A. F., Sharma, V. P., van Zyl, P. G., Beukes, J. P., Sun, J., Rohwer, E. G., Deng, R., Mamouri, R.-E., and Zamorano, F.: An overview of the first decade of Polly^{NET}: an emerging network of automated

Raman-polarization lidars for continuous aerosol profiling, Atmos. Chem. Phys., 16, 5111–5137, https://doi.org/10.5194/acp-16-5111-2016, 2016.

Baars, H., Geiß, A., Wandinger, U., Herzog, A., Engelmann, R., Bühl, J., Radenz, M., Seifert, P., Ansmann, A., Martin, A., Leinweber, R., Lehmann, V., Weissmann, M., Cress, A., Filioglou, M., Komppula, M., and Reitebuch, O.: First Results from the German Cal/Val Activities for Aeolus, EPJ Web Conf., 237, 01008, https://doi.org/10.1051/epjconf/202023701008, 2020.

Baars, H., Radenz, M., Floutsi, A. A., Engelmann, R., Althausen, D., Heese, B., Ansmann, A., Flament, T., Dabas, A., Trapon, D., Reitebuch, O., Bley, S., and Wandinger, U.: Californian Wildfire Smoke Over Europe: A First Example of the Aerosol Observing Capabilities of Aeolus Compared to Ground-Based Lidar, Geophys. Res. Lett., 48, e2020GL092194, https://doi.org/10.1029/2020GL092194, 2021.

Barton-Grimley, R. A., Nehrir, A. R., Kooi, S. A., Collins, J. E., Harper, D. B., Notari, A., Lee, J., DiGangi, J. P., Choi, Y., and Davis, K. J.: Evaluation of the High Altitude Lidar Observatory (HALO) methane retrievals during the summer 2019 ACT-America campaign, Atmos. Meas. Tech., 15, 4623–4650, https://doi.org/10.5194/amt-15-4623-2022, 2022.

Bedka, K. M., Nehrir, A. R., Kavaya, M., Barton-Grimley, R., Beaubien, M., Carroll, B., Collins, J., Cooney, J., Emmitt, G. D., Greco, S., Kooi, S., Lee, T., Liu, Z., Rodier, S., and Skofronick-Jackson, G.: Airborne lidar observations of wind, water vapor, and aerosol profiles during the NASA Aeolus calibration and validation (Cal/Val) test flight campaign, Atmos. Meas. Tech., 14, 4305–4334, https://doi.org/10.5194/amt-14-4305-2021, 2021.

Bruneau, D., Pelon, J., Blouzon, F., Spatazza, J., Genau, P., Buchholtz, G., Amarouche, N., Abchiche, A., and Aouji, O.: 355-nm high spectral resolution airborne lidar LNG: system description and first results, Appl. Optics, 54, 8776–8785, https://doi.org/10.1364/AO.54.008776, 2015.

Burton, S. P., Ferrare, R. A., Hostetler, C. A., Hair, J. W., Rogers, R. R., Obland, M. D., Butler, C. F., Cook, A. L., Harper, D. B., and Froyd, K. D.: Aerosol classification using airborne High Spectral Resolution Lidar measurements – methodology and examples, Atmos. Meas. Tech., 5, 73–98, https://doi.org/10.5194/amt-5-73-2012, 2012.

Burton, S. P., Hair, J. W., Kahnert, M., Ferrare, R. A., Hostetler, C. A., Cook, A. L., Harper, D. B., Berkoff, T. A., Seaman, S. T., Collins, J. E., Fenn, M. A., and Rogers, R. R.: Observations of the spectral dependence of linear particle depolarization ratio of aerosols using NASA Langley airborne High Spectral Resolution Lidar, Atmos. Chem. Phys., 15, 13453–13473, https://doi.org/10.5194/acp-15-13453-2015, 2015.

Carroll, B. J., Nehrir, A. R., Kooi, S. A., Collins, J. E., Barton-Grimley, R. A., Notari, A., Harper, D. B., and Lee, J.: Differential absorption lidar measurements of water vapor by the High Altitude Lidar Observatory (HALO): retrieval framework and first results, Atmos. Meas. Tech., 15, 605–626, https://doi.org/10.5194/amt-15-605-2022, 2022.

Chepfer, H., Cesana, G., Winker, D., Getzewich, B., Vaughan, M., and Liu, Z.: Comparison of Two Different Cloud Climatologies Derived from CALIOP-Attenuated Backscattered Measurements (Level 1): The CALIPSO-ST and the CALIPSO-GOCCP, J. Atmos. Ocean. Tech., 30, 725–744, https://doi.org/10.1175/JTECH-D-12-00057.1, 2013.

Collis, R. T. H. and Russell, P. B.: Lidar measurement of particles and gases by elastic backscattering and differential absorption, Springer Berlin Heidelberg, Berlin, Heidelberg, 71–151, ISBN 978-3-540-38239-3, https://doi.org/10.1007/3-540-07743-X_18, 1976.

Dabas, A., Denneulin, M.-L., Flamant, P., Loth, C., Garnier, A., and Dolfi-Bouteyre, A.: Correcting winds measured with a Rayleigh Doppler lidar from pressure and temperature effects, Tellus A, 60, 206–215, https://doi.org/10.1111/j.1600-0870.2007.00284.x, 2008.

Ehlers, F., Flament, T., Dabas, A., Trapon, D., Lacour, A., Baars, H., and Straume-Lindner, A. G.: Optimization of Aeolus' aerosol optical properties by maximum-likelihood estimation, Atmos. Meas. Tech., 15, 185–203, https://doi.org/10.5194/amt-15-185-2022, 2022.

Engelmann, R., Kanitz, T., Baars, H., Heese, B., Althausen, D., Skupin, A., Wandinger, U., Komppula, M., Stachlewska, I. S., Amiridis, V., Marinou, E., Mattis, I., Linné, H., and Ansmann, A.: The automated multiwavelength Raman polarization and water-vapor lidar Polly^{XT}: the neXT generation, Atmos. Meas. Tech., 9, 1767–1784, https://doi.org/10.5194/amt-9-1767-2016, 2016.

ESA: ESA Aeolus Online Dissemination System, ESA [data set], http://aeolus-ds.eo.esa.int/oads/access/, last access 22 May 2024.

Fehr, T., McCarthy, W., Amiridis, V., Baars, H., von Bismarck, J., Borne, M., Chen, S., Flamant, C., Marenco, F., Knipperz, P., Koopman, R., Lemmerz, C. L., Marinou, E., Močnik, G., Parrinello, T., Piña, A., Reitebuch, O., Skofronick-Jackson, G., Zawislak, J., and Zenk, C.: The Joint Aeolus Tropical Atlantic Campaign 2021/2022 Overview – Atmospheric Science and Satellite Validation in the Tropics, EGU General Assembly 2023, Vienna, Austria, 23–28 April 2023, EGU23-7249, https://doi.org/10.5194/egusphere-egu23-7249, 2023.

Feofilov, A. G., Chepfer, H., Noël, V., Guzman, R., Gindre, C., Ma, P.-L., and Chiriaco, M.: Comparison of scattering ratio profiles retrieved from ALADIN/Aeolus and CALIOP/CALIPSO observations and preliminary estimates of cloud fraction profiles, Atmos. Meas. Tech., 15, 1055–1074, https://doi.org/10.5194/amt-15-1055-2022, 2022.

Flamant, C., Chaboureau, J.-P., Delanoë, J., Gaetani, M., Jamet, C., Lavaysse, C., Bock, O., Borne, M., Cazenave, Q., Coutris, P., Cuesta, J., Menut, L., Aubry, C., Benedetti, A., Bosser, P., Bounissou, S., Caudoux, C., Collomb, H., Donal, T., Febvre, G., Fehr, T., Fink, A. H., Formenti, P., Araujo, N. G., Knippertz, P., Lecuyer, E., Andrade, M. N., Langué, C. G. N., Jonville, T., Schwarzenboeck, A., and Takeishi, A.: Cyclogenesis in the Tropical Atlantic: First Scientific Highlights from the Clouds–Atmospheric Dynamics–Dust Interactions in West Africa (CADDIWA) Field Campaign, B. Am. Meteorol. Soc., 105, E387–E417, https://doi.org/10.1175/BAMS-D-23-0230.1, 2024.

Flamant, P., Cuesta, J., Denneulin, M.-L., Dabas, A., and Huber, D.: ADM-Aeolus retrieval algorithms for aerosol and cloud products, Tellus A, 60, 273–286, https://doi.org/10.1111/j.1600-0870.2007.00287.x, 2008.

Flamant, P., Dabas, A., Martinet, P., Lever, V., Flament, T., Trapon, D., Olivier, M., Cuesta, J., and Huber, D.: Aeolus L2A Algorithm Theoretical Baseline Document, Particle optical properties product, Tech. rep., ESA, version 6.0, https://earth.esa.int/eogateway/

catalog/aeolus-l2a-aerosol-cloud-optical-product (last access: 17 January 2025), 2022.

Flament, T., Trapon, D., Lacour, A., Dabas, A., Ehlers, F., and Huber, D.: Aeolus L2A aerosol optical properties product: standard correct algorithm and Mie correct algorithm, Atmos. Meas. Tech., 14, 7851–7871, https://doi.org/10.5194/amt-14-7851-2021, 2021.

Floutsi, A. A., Baars, H., Engelmann, R., Althausen, D., Ansmann, A., Bohlmann, S., Heese, B., Hofer, J., Kanitz, T., Haarig, M., Ohneiser, K., Radenz, M., Seifert, P., Skupin, A., Yin, Z., Abdullaev, S. F., Komppula, M., Filioglou, M., Giannakaki, E., Stachlewska, I. S., Janicka, L., Bortoli, D., Marinou, E., Amiridis, V., Gialitaki, A., Mamouri, R.-E., Barja, B., and Wandinger, U.: DeLiAn – a growing collection of depolarization ratio, lidar ratio and Ångström exponent for different aerosol types and mixtures from ground-based lidar observations, Atmos. Meas. Tech., 16, 2353–2379, https://doi.org/10.5194/amt-16-2353-2023, 2023.

Freudenthaler, V., Esselborn, M., Wiegner, M., Heese, B., Tesche, M., Ansmann, A., Müller, D., Althausen, D., Wirth, M., Fix, A., Ehret, G., Knippertz, P., Toledano, C., Gasteiger, J., Garhammer, M., and Seefeldner, M.: Depolarization ratio profiling at several wavelengths in pure Saharan dust during SAMUM 2006, Tellus B, 61, 165–179, https://doi.org/10.1111/j.1600-0889.2008.00396.x, 2009.

Gebauer, H., Floutsi, A. A., Haarig, M., Radenz, M., Engelmann, R., Althausen, D., Skupin, A., Ansmann, A., Zenk, C., and Baars, H.: Tropospheric sulfate from Cumbre Vieja (La Palma) observed over Cabo Verde contrasted with background conditions: a lidar case study of aerosol extinction, backscatter, depolarization and lidar ratio profiles at 355, 532 and 1064 nm, Atmos. Chem. Phys., 24, 5047–5067, https://doi.org/10.5194/acp-24-5047-2024, 2024.

Gkikas, A., Gialitaki, A., Binietoglou, I., Marinou, E., Tsichla, M., Siomos, N., Paschou, P., Kampouri, A., Voudouri, K. A., Proestakis, E., Mylonaki, M., Papanikolaou, C.-A., Michailidis, K., Baars, H., Straume, A. G., Balis, D., Papayannis, A., Parrinello, T., and Amiridis, V.: First assessment of Aeolus Standard Correct Algorithm particle backscatter coefficient retrievals in the eastern Mediterranean, Atmos. Meas. Tech., 16, 1017–1042, https://doi.org/10.5194/amt-16-1017-2023, 2023.

Groß, S., Esselborn, M., Weinzierl, B., Wirth, M., Fix, A., and Petzold, A.: Aerosol classification by airborne high spectral resolution lidar observations, Atmos. Chem. Phys., 13, 2487–2505, https://doi.org/10.5194/acp-13-2487-2013, 2013.

Groß, S., Freudenthaler, V., Schepanski, K., Toledano, C., Schäfler, A., Ansmann, A., and Weinzierl, B.: Optical properties of long-range transported Saharan dust over Barbados as measured by dual-wavelength depolarization Raman lidar measurements, Atmos. Chem. Phys., 15, 11067–11080, https://doi.org/10.5194/acp-15-11067-2015, 2015.

Haarig, M., Ansmann, A., Althausen, D., Klepel, A., Groß, S., Freudenthaler, V., Toledano, C., Mamouri, R.-E., Farrell, D. A., Prescod, D. A., Marinou, E., Burton, S. P., Gasteiger, J., Engelmann, R., and Baars, H.: Triple-wavelength depolarization-ratio profiling of Saharan dust over Barbados during SALTRACE in 2013 and 2014, Atmos. Chem. Phys., 17, 10767–10794, https://doi.org/10.5194/acp-17-10767-2017, 2017a.

Haarig, M., Ansmann, A., Gasteiger, J., Kandler, K., Althausen, D., Baars, H., Radenz, M., and Farrell, D. A.: Dry versus wet marine particle optical properties: RH dependence of depolarization ratio, backscatter, and extinction from multiwavelength lidar measurements during SALTRACE, Atmos. Chem. Phys., 17, 14199–14217, https://doi.org/10.5194/acp-17-14199-2017, 2017b.

Haarig, M., Ansmann, A., Baars, H., Jimenez, C., Veselovskii, I., Engelmann, R., and Althausen, D.: Depolarization and lidar ratios at 355, 532, and 1064 nm and microphysical properties of aged tropospheric and stratospheric Canadian wildfire smoke, Atmos. Chem. Phys., 18, 11847–11861, https://doi.org/10.5194/acp-18-11847-2018, 2018.

Haarig, M., Ansmann, A., Engelmann, R., Baars, H., Toledano, C., Torres, B., Althausen, D., Radenz, M., and Wandinger, U.: First triple-wavelength lidar observations of depolarization and extinction-to-backscatter ratios of Saharan dust, Atmos. Chem. Phys., 22, 355–369, https://doi.org/10.5194/acp-22-355-2022, 2022.

Hair, J. W., Hostetler, C. A., Cook, A. L., Harper, D. B., Ferrare, R. A., Mack, T. L., Welch, W., Izquierdo, L. R., and Hovis, F. E.: Airborne High Spectral Resolution Lidar for profiling aerosol optical properties, Appl. Optics, 47, 6734–6752, https://doi.org/10.1364/AO.47.006734, 2008.

Hofer, J., Althausen, D., Abdullaev, S. F., Makhmudov, A. N., Nazarov, B. I., Schettler, G., Engelmann, R., Baars, H., Fomba, K. W., Müller, K., Heinold, B., Kandler, K., and Ansmann, A.: Long-term profiling of mineral dust and pollution aerosol with multiwavelength polarization Raman lidar at the Central Asian site of Dushanbe, Tajikistan: case studies, Atmos. Chem. Phys., 17, 14559–14577, https://doi.org/10.5194/acp-17-14559-2017, 2017.

Hunter, J. D.: Matplotlib: A 2D graphics environment, Comput. Sci. Eng., 9, 90–95, https://doi.org/10.1109/MCSE.2007.55, 2007.

Illingworth, A. J., Barker, H. W., Beljaars, A., Ceccaldi, M., Chepfer, H., Clerbaux, N., Cole, J., Delanoë, J., Domenech, C., Donovan, D. P., Fukuda, S., Hirakata, M., Hogan, R. J., Huenerbein, A., Kollias, P., Kubota, T., Nakajima, T., Nakajima, T. Y., Nishizawa, T., Ohno, Y., Okamoto, H., Oki, R., Sato, K., Satoh, M., Shephard, M. W., Velázquez-Blázquez, A., Wandinger, U., Wehr, T., and van Zadelhoff, G.-J.: The EarthCARE Satellite: The Next Step Forward in Global Measurements of Clouds, Aerosols, Precipitation, and Radiation, B. Am. Meteorol. Soc., 96, 1311–1332, https://doi.org/10.1175/BAMS-D-12-00227.1, 2015.

Khaykin, S., Podglajen, A., Ploeger, F., Grooß, J.-U., Tence, F., Bekki, S., Khlopenkov, K., Bedka, K., Rieger, L., Baron, A., Godin-Beekmann, S., Legras, B., Sellitto, P., Sakai, T., Barnes, J., Uchino, O., Morino, I., Nagai, T., Wing, R., Baumgarten, G., Gerding, M., Duflot, V., Payen, G., Jumelet, J., Querel, R., Liley, B., Bourassa, A., Clouser, B., Feofilov, A., Hauchecorne, A., and Ravetta, F.: Global perturbation of stratospheric water and aerosol burden by Hunga eruption, Commun. Earth Environ., 3, 316, https://doi.org/10.1038/s43247-022-00652-x, 2022.

Lemmerz, C., Witschas, B., Lux, O., Rahm, S., Schmidt, K., Marksteiner, U., Geiß, A., Schäfler, A., Weiler, F., and Reitebuch, O.: Validation campaigns for Aeolus with the ALADIN Airborne Demonstrator and 2-µm Doppler wind lidar team, in: 21st Coherent Laser Radar Conference (CLRC-21), 26 June–1 July 2022, Big Sky, Montana, USA, https://elib.dlr.de/199958/ (last access: 9 May 2024), 2023.

Lux, O., Lemmerz, C., Sanctis, V. D., Bravetti, P., Wernham, D., Krisna, T. C., Parrinello, T., and Reitebuch, O.: Performance of the ultraviolet laser transmitter during ESA's Doppler wind lidar mission Aeolus, Appl. Optics, 63, 9315–9336, https://doi.org/10.1364/AO.544577, 2024.

NASA/LARC/SD/ASDC: CPEX-CV HALO Aerosol and Water Vapor Profiles and Images, NASA Langley Atmospheric Science Data Center DAAC [data set], https://doi.org/10.5067/ASDC/SUBORBITAL/CPEXCV-HALO_DC8_1, 2023.

Nehrir, A., Notari, A., Harper, D., Fitzpatrick, F., Collins, J., Kooi, S., Antill, C., Hare, R., Barton-Grimley, R., Hair, J., Ferrare, R., Hostetler, C., and Welch, W.: The High Altitude Lidar Observatory (HALO): A multi-function lidar and technology test-bed for airborne and space-based measurements of water vapor and methane, earth Science Technology Forum, 12–14 June 2018, Silver Spring, Maryland, USA, https://esto.nasa.gov/techportfolio//pdf/additionalInfo/1914_Nehrir/Nehrir_ESTF2018_A1P2.pdf (last access: 26 May 2023), 2018.

Nehrir, A. R., Kiemle, C., Lebsock, M. D., Kirchengast, G., Buehler, S. A., Löhnert, U., Liu, C.-L., Hargrave, P. C., Barrera-Verdejo, M., and Winker, D. M.: Emerging Technologies and Synergies for Airborne and Space-Based Measurements of Water Vapor Profiles, Surv. Geophys., 38, 1445–1482, 2017.

Nowottnick, E. P., Rowe, A. K., Nehrir, A. R., Zawislak, J. A., Piña, A. J., McCarty, W., Barton-Grimley, R. A., Bedka, K. M., Bennett, J. R., Brammer, A., Buzanowicz, M. E., Chen, G., Chen, S.-H., Chen, S. S., Colarco, P. R., Cooney, J. W., Crosbie, E., Doyle, J., Fehr, T., Ferrare, R. A., Harrah, S. D., Hristova-Veleva, S. M., Lambrigtsen, B. H., Lawton, Q. A., Lee, A., Marinou, E., Martin, E. R., Močnik, G., Mazza, E., Monje, R. R., Ocasio, K. M. N., Pu, Z., Rajagopal, M., Reid, J. S., Robinson, C. E., Rios-Berrios, R., Rodenkirch, B. D., Sakaeda, N., Salazar, V., Shook, M. A., Sinclair, L., Skofronick-Jackson, G. M., Thornhill, K. L., Torn, R. D., Gilst, D. P. V., Veals, P. G., Vömel, H., Wong, S., Wu, S.-N., Ziemba, L. D., and Zipser, E. J.: Dust, Convection, Winds, and Waves: The 2022 NASA CPEX-CV Campaign, B. Am. Meteorol. Soc., 105, E2097–E2125, https://doi.org/10.1175/BAMS-D-23-0201.1, 2024.

Paschou, P., Siomos, N., Tsekeri, A., Louridas, A., Georgoussis, G., Freudenthaler, V., Binietoglou, I., Tsaknakis, G., Tavernarakis, A., Evangelatos, C., von Bismarck, J., Kanitz, T., Meleti, C., Marinou, E., and Amiridis, V.: The eVe reference polarisation lidar system for the calibration and validation of the Aeolus L2A product, Atmos. Meas. Tech., 15, 2299–2323, https://doi.org/10.5194/amt-15-2299-2022, 2022.

Reitebuch, O., Krisch, I., Lemmerz, C., Lux, O., Schmidt, K., Witschas, B., Marksteiner, U., Rennie, M., Nikolaus, I., Fabre, F., Trapon, D., Dabas, A., Donovan, D., van Zadelhoff, G.-J., Wang, P., Marseille, G.-J., Kuijt, A., Tagliacarne, F., Perron, G., Huber, D., Meringer, M., Reissig, K., de Kloe, J., Cardaci, M., Gostinicchi, G., McLean, W., Henry, K., Benedetti, A., Bley, S., Stoffelen, A., Sabbatini, P., Mahfouf, J.-F., and Pourret, V.: The Earth Explorer Mission Aeolus for atmospheric wind observations – Final report from the Aeolus Data Innovation and Science Cluster DISC of Phase E, Tech. rep., ESA, https://elib.dlr.de/209970/ (last access: 17 January 2025), 2024.

Ridgway, G.: Bipolar Colormap, MATLAB Central File Exchange [code], https://www.mathworks.com/matlabcentral/fileexchange/26026-bipolar-colormap, last access: 17 January 2025.

Rittmeister, F., Ansmann, A., Engelmann, R., Skupin, A., Baars, H., Kanitz, T., and Kinne, S.: Profiling of Saharan dust from the Caribbean to western Africa – Part 1: Layering structures and optical properties from shipborne polarization/Raman lidar observations, Atmos. Chem. Phys., 17, 12963–12983, https://doi.org/10.5194/acp-17-12963-2017, 2017.

Trapon, D., Flament, T., Lacour, A., and Stieglitz, H.: Aeolus L2A user guide, Tech. rep., ESA, version 2.2, https://earth.esa.int/eogateway/documents/20142/37627/Aeolus-Data-Innovation-Science-Cluster-DISC-Level-2A-user-guide.pdf (last access: 20 May 2023), 2022.

Turk, F. J., Hristova-Veleva, S., Durden, S. L., Tanelli, S., Sy, O., Emmitt, G. D., Greco, S., and Zhang, S. Q.: Joint analysis of convective structure from the APR-2 precipitation radar and the DAWN Doppler wind lidar during the 2017 Convective Processes Experiment (CPEX), Atmos. Meas. Tech., 13, 4521–4537, https://doi.org/10.5194/amt-13-4521-2020, 2020.

Winker, D. M., Vaughan, M. A., Omar, A., Hu, Y., Powell, K. A., Liu, Z., Hunt, W. H., and Young, S. A.: Overview of the CALIPSO Mission and CALIOP Data Processing Algorithms, J. Atmos. Ocean. Tech., 26, 2310–2323, https://doi.org/10.1175/2009JTECHA1281.1, 2009.

Zawislak, J., Nowottnick, E., and Nehrir, A.: Convective Processes Experiment – Cabo Verde (CPEX-CV) Field Campaign Collection [High Altitude Lidar Observatory (HALO) CPEX-CV], NASA EOSDIS Global Hydrometeorology Resource Center Distributed Active Archive Center, Huntsville, Alabama, USA, https://doi.org/10.5067/CPEXCV/DATA101, 2022.

Zhu, C., Byrd, R. H., Lu, P., and Nocedal, J.: Algorithm 778: L-BFGS-B: Fortran subroutines for large-scale bound-constrained optimization, ACM Trans. Math. Softw., 23, 550–560, https://doi.org/10.1145/279232.279236, 1997.